



UNIVERSIDADE DA BEIRA INTERIOR  
Engenharia

## **Development of an Efficient Propulsion System for a Battery Electric Shell Eco Marathon Prototype Vehicle**

Versão final após defesa

**Jorge Miguel Guedes Rebelo**

Dissertação para obtenção do Grau de Mestre em  
**Engenharia Aeronáutica**  
(Ciclo de estudos integrado)

Orientador: Prof. Doutor Miguel Ângelo Rodrigues Silvestre

Covilhã, julho de 2017



## Dedication

The author dedicates his dissertation work to his family and many friends. A special feeling of gratitude to his loving parents, Rui and Maria José whose words of encouragement and push for tenacity ring in his ears. His sister Catarina, have never left his side.

The author also dedicates this dissertation to his many friends and work colleagues who have supported him throughout the process. The author always appreciated all they have done, especially professor Miguel Silvestre for helping the development of the author's theoretical and practical skills.

The author dedicates this work and give special thanks to his girlfriend for being there throughout the entire master program.



# Acknowledgements

The author would like to thank Professor Miguel Silvestre for supervising, for his suggestions and guidelines through this project. this project would not have been possible without his knowledge and skills.

The author is also thankful to all professors for their dedication to quality engineering instruction, for serving on his graduate committee, and for tying up the ends of the degree on such short notice.

And to all team members of Aero@UBI team for the team-work and experiences shared during this project.

The author would also like to thanks to everyone involved for being patient, understanding, and willing to work with him through the tough spots and delays in the work as well as those in his own life.

Last but not the least, the author would like to thank to the “Top Team” from Heliportugal for giving the permission and the time for the accomplishment of this thesis and encouragement, as well.



# Resumo

Para a participação da equipa Aero@Ubi na competição da Shell Eco-marathon, um motor elétrico de imanes permanentes, sem núcleo ferromagnético, foi desenhado, construído e testado. Este tipo de motor é caracterizado por ter uma baixa indutância e baixa resistência elétrica o que provoca picos de corrente quando acionado. Para resolver este problema, e também como requisito do regulamento da prova um controlador deve ser desenvolvido. Neste caso, foi desenvolvido, construído e testado um controlador com uma comutação de 60 graus.

## Palavras-chave

**Motor elétrico, magnetos permanentes, sem ferro, controlador de motor, comutação de 60 graus.**



## **Abstract**

For the participation of the Aero@UBI team in Shell Eco-Marathon competition an in-wheel electric, ironless brushless permanent magnet motor was designed and build, this type of motors is characterized by very inductance and a very low resistance between phases which leads to current ripple, to solve this problem, and also, as Shell Eco-marathon competition requirements, a controller must be developed. In this case a controller with a 60-degree commutation was implemented and tested.

## **Keywords**

Electric motor, permanent magnet, ironless, motor controller, 60-degree commutation.



# Table of Contents

Chapter 1	1
1.1. Motivation	1
1.2. Scope	2
1.3. Objectives	2
1.4. Dissertation structure	3
Chapter 2	5
2.1. Definitions and types of brushless motors	5
2.1.1. Basic Terminology	5
2.1.2. Motor Losses and Efficiency	7
2.1.3. Back Electromotive Force and Torque Production	7
2.2. Motor Controllers	8
2.2.1. Three Phase Motor Commutation Scheme	9
2.2.1.1. Trapezoidal Commutation	9
2.2.1.2. Sinusoidal Commutation	10
2.2.2. Phase Current Level Control	11
2.2.2.1. PWM Current Control	11
2.2.2.2. Hysteretic Phase Current Control	13
2.2.2.3. Multilevel Inverter for Phase Current Control	13
2.2.2.4. Field Oriented Control	16
2.3. State of the Art	17
2.3.1. PMSM Electrical Machines	17
2.3.2. Motor Controller	20
Chapter 3	23
3.1. Motor Development	23
3.1.1. Conceptual Design	23
3.1.2. Preliminary Design	28
3.1.3. Detailed Design	34
3.1.4. Fabrication	35
3.1.4.1. Stator	35
3.1.4.2. Rotor Manufacture Process	37
3.1.4.3. Stator Support	37
3.1.4.4. Wheel/Motor Hub	38
3.1.5. Motor Testing	39
3.1.5.1. Back Electromotive Force	39
3.1.5.2. Motor Mechanical Losses Measurements	39
3.1.5.2.1. Motor Rotor's Moment of Inertia Measurements	39
3.1.5.2.2. Mechanical Losses Measurement	40
3.2. Controller Development	40

3.2.1. Conceptual design	40
3.2.2. Circuit Design and Component Selection	43
3.2.2.1. Half-Bridge Module	43
3.2.2.1.1. Gate Drive Optocoupler	43
3.2.2.1.2. Shoot-Through Protection	44
3.2.2.1.3. MOSFET	45
3.2.2.1.4. Bootstrap	46
3.2.2.1.5. Bus Capacitor	46
3.2.2.2. Current Sensor and Comparator Module	46
3.2.2.2.1. Current Sensor	47
3.2.2.2.2. Current Comparator	47
3.2.2.2.3. PLD Module	47
3.2.2.3.1. Motor Position	48
3.2.2.3.4. Capacitor Bank Module	48
3.2.3. Implementation	48
3.2.3.1. Half-Bridge Module	49
3.2.3.2. Current Sensor and Comparator Module	50
3.2.3.3. PLD module	51
3.2.3.3.1. Motor Position Sensors	52
3.2.3.4. Capacitor Bank Module	52
3.2.4. Controller Testing	53
3.2.4.1. Current Limiting Function	53
3.2.5. Controller and Motor Testing	54
3.2.5.1. No Load Current	54
3.2.5.2. Loaded System Testing	54
3.2.5.3. Load Testing with TI C2000 and DRV8301Controller	55
Chapter 4	57
4.1. Motor Testing	57
4.1.1. Back Electromotive Force	57
4.1.2. Motor Mechanical Losses	58
4.1.2.1. Motor Rotor's Moment of Inertia	58
4.1.2.2. Motor Mechanical Losses Measurement	59
4.2. Controller Testing	59
4.2.1. Current Limiting Function	59
4.3. Controller and Motor Testing	60
4.3.1. No Load Current	60
4.3.2. Load Current	61
4.3.3. Load TI C2000 and DRV8301	62
4.3.4. SEM Vehicle Prototype on Track Performance	63
Chapter 5	65

# Figure list

Figure 1 - Aero@UBI01 in SEM 2015 competition run	1
Figure 2 - Basic permanent magnet synchronous motor	5
Figure 3 - Motor configurations: radial flux inrunner rotor, radial flux outrunner rotor and axial flux disk rotor	6
Figure 4 - Sinusoidal and trapezoidal BEMF waveforms [3]	8
Figure 5 - Typical Controller architecture	9
Figure 6 - Current path on a trapezoidal commutation [4]	10
Figure 7 - Current path on a sinusoidal commutation [4]	10
Figure 8 - Typical analog PWM Inverter	12
Figure 9 - Typical Hysteresis Current Controller [5]	13
Figure 10 - Multilevel Inverter Output [6] a) two-level inverter, b) three-level inverter and c) nine-level inverter.	14
Figure 11 - Multilevel inverter representation with: two levels a), three levels b), and n levels c)[7]	14
Figure 12 - Three-level inverter: a) basic circuit; b) implemented in a diode clamped topology; c) implemented in a flying capacitor topology adapted from [7]	15
Figure 13 - Castaded half-bridge inverter [7]	16
Figure 14 - Field Oriented Control Implementation [8]	16
Figure 15 -Field Oriented Control Implementation [9]	17
Figure 16 - Motor CSIRO [12]	18
Figure 17 - LaunchPoint's Electric Motor [14]	19
Figure 18 - Layout of the motor drive control system presented by Caricchi et al [10]	21
Figure 19 - Wave winding concept	26
Figure 20 - Motor axial flux coreless motor concept	26
Figure 21 - Motor section concept	27
Figure 22 - First motor concept design.	27
Figure 23 - Motor stator copper mass due to pole count in function of design point efficiency	33
Figure 24 - Motor mass versus design point efficiency.	33
Figure 25 - Final motor design	35
Figure 26 - Stator design	35
Figure 27 - Phase winding markings	36
Figure 28 - Stator fabrication before pouring the epoxy resin.	36
Figure 29 - Rotor fabrication - placing the magnets	37
Figure 30 - Stator Support	38
Figure 31 - Wheel/Motor Hub	38

Figure 32 - Moment of Inertia Measurement: Test rig schema to measure the motor rotor's moment of inertia.	40
Figure 33 - Graphical representation of the 60-degree commutation scheme	42
Figure 34 - First controller concept design	43
Figure 35 - Shoot-through protection circuit	44
Figure 36 - Electrical symbol of an N-channel and P-channel MOSFETs	45
Figure 37 - Bootstrap Operation	46
Figure 38 - Half-Bridge Module Schematic	49
Figure 39 - Half-Bridge Module board layout(left) and built(right).	49
Figure 40 - Current Sensor and Comparator Module Schematic.	50
Figure 41 - Current Sensor and Comparator Module layout(left) and built(right).	50
Figure 42 - PLD Module Schematic.	51
Figure 43 - PLD module layout(left) and assembled(right)	51
Figure 44 - Hall Effect Sensors positioning.	52
Figure 45 - Capacitor Bank Assembled	53
Figure 46 - Motor-Controller system test rig schematic.	53
Figure 47 - Schematic of the test bench used for load measurements	54
Figure 48 - BEMF measurement	57
Figure 49 - Measured voltage waveform vs sinusoidal waveform	58
Figure 50 - Motor of inertia measurement test rig according to section 3.1.5.2.1	58
Figure 51 - Current limiting function measurements	60
Figure 52 - No load current measurement	60
Figure 53 - Motor-Controller system efficiency experimental results with no load	61
Figure 54 - Load current measurement	61
Figure 55 - Motor-Controller system efficiency experimental results of the designed controller	62
Figure 56 - Motor-Controller system efficiency experimental results comparison between TI DRV and the designed controller	62

# Table list

Table 1 - Switching sequence for trapezoidal commutation	10
Table 2 - Switching sequence for sinusoidal commutation	11
Table 3 - Motor requirements	24
Table 4 - Motor Parameters	34
Table 5 - Switching sequence for 60-degree commutation	42
Table 6 - Specifications for the Avago ACPL-H342 Optocoupler	44
Table 7 - Specifications for the AUIRFS8409-7P N-channel MOSFET	45
Table 8 - ACS770-50U IC specifications	47
Table 9 - Rotor's moment of inertia measurements	59
Table 10 - Motor mechanical losses measurements	59



# List of Abbreviations

<b>3D</b>	Three-dimensional
<b>AC</b>	Alternating Current
<b>AFPM</b>	Axial Flux Permanent-Magnet
<b>BEMF</b>	Back Electromotive Force
<b>BLDC</b>	Brushless Direct Current
<b>CAD</b>	Computer-Aided Design
<b>CNC</b>	Computer Numeric Control
<b>CSIRO</b>	Commonwealth Scientific and Industrial Research Organization
<b>DC</b>	Direct Current
<b>EMF</b>	Electromotive Force
<b>FOC</b>	Field Oriented Control
<b>GND</b>	Ground
<b>IGBT</b>	Insulated-Gate Bipolar Transistor
<b>MsC</b>	Master of Science
<b>MOSFET</b>	Metal-Oxide-Semiconductor Field-effect Transistor
<b>PCB</b>	Printed Circuit Board
<b>PM</b>	Permanent Magnet
<b>PMSM</b>	Permanent Magnet Synchronous Motor
<b>PMG</b>	Permanent Magnet Generator
<b>PLA</b>	Polylactic Acid
<b>PLD</b>	Programmable Logic Device
<b>PWM</b>	Pulse-Width Modulation
<b>RC</b>	Radio Controlled
<b>rpm</b>	Revolutions per minute
<b>SEM</b>	Shell Eco-marathon
<b>TI</b>	Texas Instruments
<b>TTL</b>	Transistor-transistor logic
<b>VCC</b>	Positive Supply Voltage
<b>VDC</b>	Voltage in Direct Current Bus



# List of Symbols

$A$	Wave winding coil area subjected to the magnetic flux
$A_N$	Minimum copper coil wire section area
$A_S$	Stator disk area
$B_{coil}$	Flux density at the stator
$B_{mag}$	Flux intensity of the magnets
$C_s$	Shoot-through Capacitor capacitance
$d$	Direct axis
$d_{wire}$	Minimum copper wire diameter
$F_F$	Stator filling factor
$g$	Distance between opposing magnets faces
$I$	Moment of inertia
$I_A$	Current on phase A
$I_B$	Current on phase B
$I_C$	Current on phase C
$I_{ABC,rms}$	Motor phase current
$I_{rms}$	Motor current rms
$K_t$	Motor constant
$L$	Inductance
$L_{mag}$	Magnet pole length
$l_N$	Total wire length per coil
$lp$	Length of coil wire per turn
$m_{wire}$	Motor stator copper mass for the required copper volume per phase
$m_{mag}$	Stator magnets mass
$N$	Required turns per coil
$P$	Magnet poles number
$P_c$	Shaft Power
$P_{ce}$	Motor electrical power
$p_{er}$	Motor stator mean perimeter
$p_{er,in}$	Stator inner perimeter
$p_{er,out}$	Stator outer perimeter
$q$	Quadrature axis
$R$	Winding resistance
$R_{mag}$	Radius at magnets
$R_s$	Current-limiting resistor
$t_{delay}$	Shoot-through protection time delay
$t_m$	Magnet thickness

$t_{mag}$	Duration of the coil motion from one magnet to the next
$t_s$	Stator thickness
$U$	Voltage applied to the motor
$U_{ABC}$	Maximum phase voltage
$U_{ABrms}$	AC tension rms
$U_{bemfrms}$	Required motor effective back electromotive force
$U_{DC}$	Voltage of the DC bus
$U_{emf}$	Motor back electromotive force
$U_{rsw}$	Reference sinusoidal wave signal
$U_{tw}$	Triangular wave signal in the negative terminal
$V_{DC+}$	Positive voltage of DC bus
$V_{DC-}$	Negative voltage of DC bus
$V_f$	Optocoupler led forward voltage
$V_{sig}$	Voltage input in half-bridge
$V_{wire}$	Minimum copper volume per phase
$W$	Magnet pole width
$\eta_c$	Motor Efficiency
$\phi$	Magnetic flux
$\theta$	Angle corresponding to half electric revolution
$\omega$	Angular speed





# Chapter 1

## 1. Introduction

### 1.1. Motivation

Shell Eco-marathon (SEM) is a global competition that challenges student teams around the world to design, build, test and drive ultra-energy-efficient vehicles, this competition is divided in three events by the locations of the teams (Europe, Asia and Americas). There are two categories: Urban Concept and Prototype, in both categories the car design and features have some limitations, such as maximum dimensions, a purpose-built motor controller and safety features.

Although, Aeronautical Engineering students, normally deal with aircraft stuff and therefore University of Beira Interior (UBI) participated and won the Air Cargo Challenge 2011, we felt that we can bring some of our aircraft's design and build expertise into the SEM competition. In September of 2013, it was decided to apply for the European edition with a Prototype and thus, we started to gather some ideas and concepts for the design of our car. In January, we had the confirmation that the participation application was accepted and the Aero@UBI team from UBI was created and started the work on the Aero@UBI01 SEM prototype car. The same car was used in the 2014 through 2017 SEM editions. Figure 1 shows the Aero@UBI01 car from 2015 running for the Shell Eco-marathon score completion.



Figure 1 - Aero@UBI01 in SEM 2015 competition run

## **1.2. Scope**

With the participation in SEM, an opportunity was created to design, built and test an efficiency optimized electric motor and controller set from scratch, this was a great opportunity to explore a leading-edge field of study, because efficient electric propulsion is currently in the spot light, from a hobby RC Quadcopter to a road legal Electric Vehicle.

The goal of this Thesis is the development construction of an ultra-efficient propulsion system for the Aero@UBI01 SEM prototype. Since, on one hand, the motor efficiency is highly dependent on the controller ability to correctly supply the appropriate waveform that maximizes the working motor efficiency. On the other hand, if all effort would be put into supplying the correct waveform, the controller itself could suffer from excessive switching losses. Additionally, as part of the Shell Eco-marathon requirements the motor controller had to be purpose built. For all these reasons, the current work is dedicated to both the motor and the controller such that the whole propulsion system can be as efficient as possible.

## **1.3. Objectives**

The purpose of this work was to develop an in-wheel direct-drive permanent motor and respective controller for the Aero@UBI car, to do so it was necessary to:

- do a literature review to check that this was the best motor type and configuration for our purpose;
- develop a formulation to model the motor;
- identify the design parameters affecting the motor efficiency;
- implement it in a computer model to predict the motor performance;
- perform a parametric study to select a design point;
- design the motor in detail in a 3D CAD environment;
- fabricate the motor in-house using fast prototyping CNC technology;
- test the motor with a commercial controller and with the in-house developed controller.

At the same time the work on the controller included:

- a literature review about motor controllers;
- select the best control strategy for the type of motor being developed;
- implement the control in an appropriate circuit;
- select the electronic components;
- design and build the PCB;
- assemble the controller;
- test the controller with the developed motor.

## **1.4. Dissertation structure**

Beyond the present introductory chapter, this dissertation is organized into the following chapters:

- Chapter 2 presents the literature review on both the motor and the controller. It includes a review on the basic principles of operation followed by the state of the art.
- Chapter 3 presents the methodology that was implemented for the motor development in the first part and for the controller in the second part.
- Chapter 4 is where the results are presented and discussed;
- Chapter 5 is a summary of the conclusions and presents recommendations for future work.



# Chapter 2

## 2. Literature Review

This chapter will first cover the basic principles of electric motors and controllers. In respect to the first topic, the focus is narrowed to the permanent magnet synchronous motor (PMSM) since it was found to be the potentially most efficient motor type for our purpose. Next, the focus changes for the controller: describing the possible control strategies. Finally, the state of the art in the ultra-efficient electric propulsion will be presented, regarding both the electrical machine and the controller.

### 2.1. Definitions and types of brushless motors

As the name suggests, a brushless motor is a motor without brushes, slip rings or any other mechanical commutators, like it would be used in a conventional DC motor. Brushless DC motors are normally characterized by having a trapezoidal back electromotive force (BEMF) and are normally driven by rectangular pulse currents. PMSM differ from brushless DC motor in that they typically have a sinusoidal BEMF and are driven by sinusoidal currents. In reality, both brushless DC and PMSM have a BMEF more or less close to sinusoidal. But, when driven by a current matching its BEMF waveform a motor reaches a higher efficiency. So, for the current purpose, we consider brushless DC and PMSM as equivalent electric machines in terms of working principle.

#### 2.1.1. Basic Terminology

Motor configurations and categories can vary between different brushless DC or PMSM motors but they share the same internal components and principle of work.

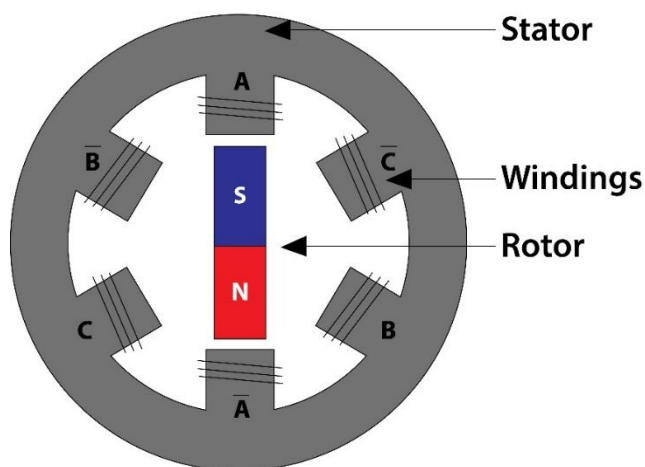


Figure 2 - Basic permanent magnet synchronous motor

Figure 2 shows a three-phase brushless DC or PMSM electric motor topology and will be used to explain the main components of a brushless electric motor. A PMSM consists contains two primary parts. The nonmoving or stationary part is called the stator, and the moving or rotating part is the rotor, that rotates with respect to the stator. The stator carries the windings and the rotor carries the magnets. The space between the stator and the rotor is the air gap. Normally, the stator of motor is a laminated silicon steel structure called the iron core, this structure has slots where the winding coils are placed. The purpose of using a ferrous core is to channel the magnetic flux in the coils. The section between two slots is called a tooth. A phase is an individual group of windings and each phase is isolated from the other two. The motor shown in this Figure 2 has concentrated coils windings but an alternative construction can be the use of distributed windings where the coils of each phase overlap. In a PMSM any even number of rotor magnet poles and any number of phases greater than one can be used.

The motor has a characteristic constant,  $K_t$ , that is the amount of torque it creates per unit electric current. This is equal to the BEMF per unit angular [1]. In order to create a higher motor constant a greater number of magnet poles should be used [2].

In electric motors, it is important to differentiate mechanical angles motion from electrical angles. Mechanical angle is the physical angle that the rotor makes in relation to the stator when it moves. If the rotor moves one complete revolution, it travels 360 mechanical degrees or  $2\pi$  mechanical radians. The Electrical angle corresponds to 360 degrees between the BEMF waveform peaks. So, the electrical angle is related to the mechanical angle by the number of magnet pole pairs. This means that if the motor has  $n$  pole pairs, the BEMF electrical angle is  $n$  times higher than the mechanical angle.

In Figure 3 is shown the two basic configurations of electric motors, they can be radial flux or axial flux motors. In the radial flux motors, there are two possible concepts in respect to the rotor: inrunner or outrunner.

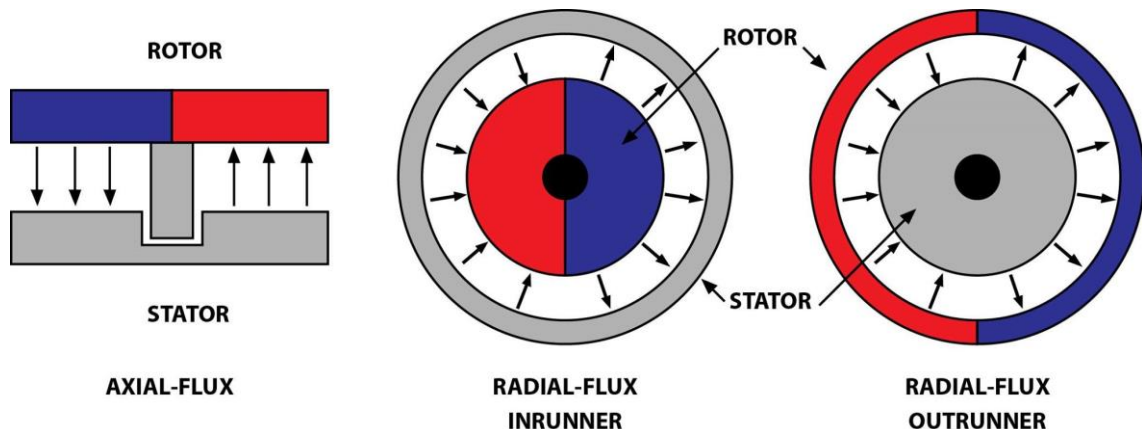


Figure 3 - Motor configurations: radial flux inrunner rotor, radial flux outrunner rotor and axial flux disk rotor

### **2.1.2.Motor Losses and Efficiency**

The losses in the motor are:

- Stator core losses;
- Windings working current Joule losses.

The stator core losses are divided in magnetic hysteresis, that produces heat when changing the magnetization of the core, and induced currents (Eddy-currents) in the core, due to the core being normally conductive.

Normally, the most important share of losses in a typical brushless motor working at low driving currents is the core loss, due to Eddy-currents and magnetic hysteresis in the rotor core laminations. Normally, the core losses are minimized by the use of low hysteresis silicone steel in individually isolated layers forming a laminated structure perpendicular to the magnetic flux.

One possible way of reducing core losses would be the use of the non-conductive ferrite like core materials such that these Eddy-currents would not occur but the production of such desired geometries in ferrite is not straightforward. Another way of getting rid of the core losses is to get rid of the core itself. One problem that arises from a coreless motor is that the magnets' flux will run through the windings unchanneled by the lack of the core tooth. In this case, the Eddy-currents in the windings can be minimized by using parallel strands of individually insulated thin wires (Litz wire).

The stator windings produce losses whenever they carry current to produce torque. The winding losses or  $I^2R$  losses are due to the current flowing through the conductors of the motor. These losses are equal to the square of the current times the resistance of the path through which the current flows. At low speeds such as in an in-wheel motor, the  $I^2R$  or the copper loss can be higher than the core losses.

### **2.1.3.Back Electromotive Force and Torque Production**

When the phases of a PMSM are energized and the current flows through them, torque is produced and makes the motor rotate. With the motor rotation, the rotor's magnets change positions and the flux linkage changes, which induces a voltage on the phases according to Faraday's law. This induced voltage is called Back Electromotive Force (BEMF) and it is, according to Lenz's Law, opposite to the current that causes it. The magnitude of the BEMF is thus proportional to the frequency of the motor, so, if the motor is driven by a constant voltage, as the motor accelerates the magnitude of the phase current decreases. If the motor is running empty, it will stop its acceleration when the BEMF is equal to the supplied voltage, at this point, if no load is applied to the motor, the energy consumed is only due to mechanical losses.

The BEMF waveform is determined by the distribution of the flux in the air gap, that is dependent of the winding arrangement of the phases and the magnets positions. Figure 4 shows two BEMF waveforms a trapezoidal shaped BEMF is a characteristic of Brushless DC motors while the PMSM are characterized by having a sinusoidal BEMF.

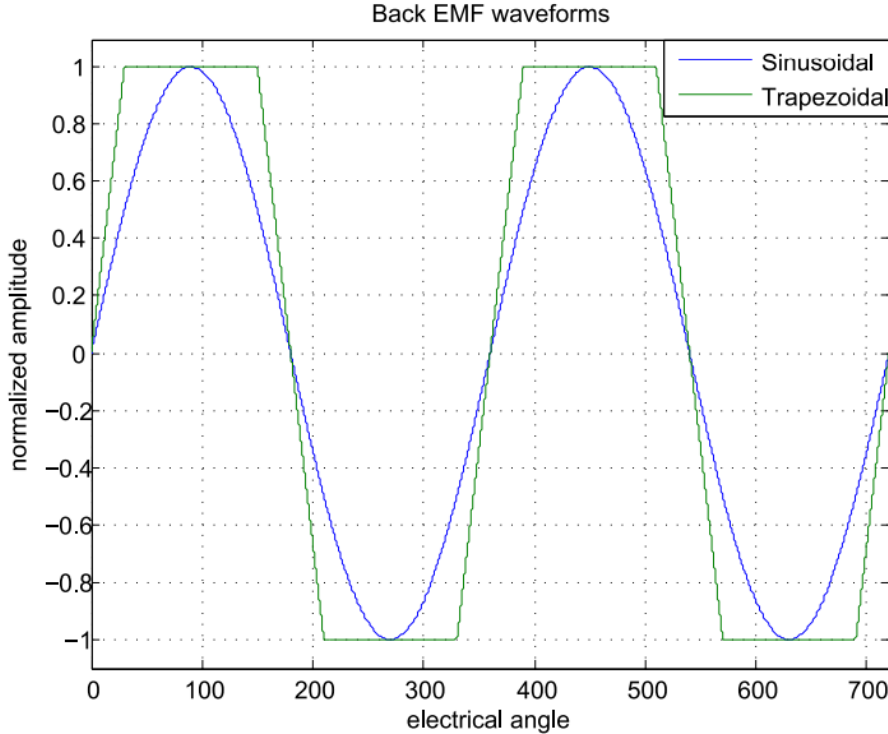


Figure 4 - Sinusoidal and trapezoidal BEMF waveforms [3]

## 2.2. Motor Controllers

The control strategy is a set of rules or algorithms that govern when and how the electronic power switches are turned on and off. The control strategy objective is to give smooth and accurate control of torque and speed, therefore the current level is limited in such a way that the motor efficiency is maximized. PMSM requires alternating phase currents that should be ideally replicate the motor's BEMF. Typically, a sinewave. This allows for maximum efficiency, since current is supplied when it results in torque. If current is supplied to the coil when the magnet pole is aligned with it, i.e., when the phase BEMF is zero, the torque will be zero and all the supplied energy is wasted. In the case of a three-phase motor, each phase sine wave signal must be 120 electrical degrees out of phase relative to each other since this allows constant torque.

Typically, a PMSM controller can be divided in three modules (see Figure 5): motor electrical position sensing for correct phase commutation (equivalent to the brushes function in brushed motors; gate driving module and the gates themselves. In the first module, besides commutating to supply current in phase with the phase's BEMF, the shape of the current

function should be modulated to replicate the BEMF itself. This is called the control strategy. Since the current function must be generated from a DC bus, a Pulse-Width Modulation (PWM) is normally used to control the current level (motor torque level control) and the current function shape in the respect to the motor electrical position. The second module only converts the digital logic electrical signal to a suitable gate operation power supply. The third module is responsible for connecting the phase terminal to the DC bus + or - terminal and disconnecting the phase when required. For this, electronic power switches are used: MOSFETs or IGBTs. MOSFETs are preferred when low DC bus voltages are used because they have a smaller resistance for the lower limit operation voltage. IGBTs have constant voltage drop which translate to lower relative power losses as the operating DC bus voltage increases.

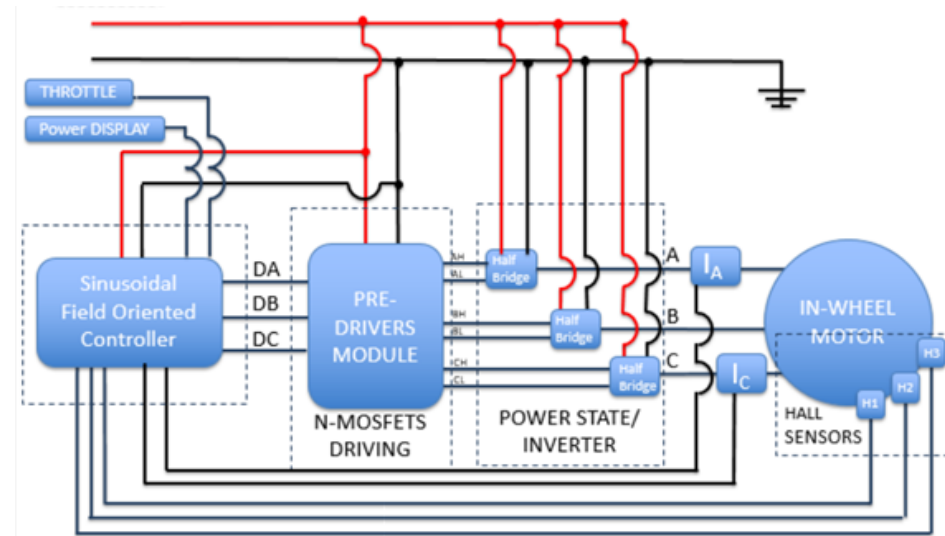
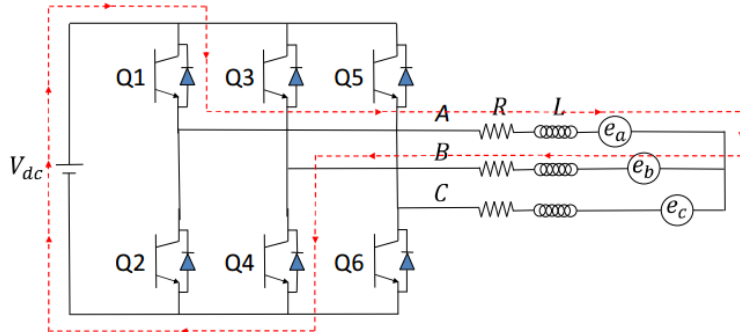


Figure 5 - Typical Controller architecture

### 2.2.1.Three Phase Motor Commutation Scheme

#### 2.2.1.1. Trapezoidal Commutation

PMSM are very similar to BLDC motors. The only difference being that the later type is supposed to have a trapezoidal BEMF. So, the commutation is necessary to generate AC from a DC bus. Nevertheless, the simplest way to commutate a PMSM motor from a DC bus is through the trapezoidal commutation. In this case a PMSM is working, in fact, as a BLDC motor. In this scheme, the current is controlled through motor terminals one pair at a time and having the third motor terminal disconnected (Figure 6). It uses six different stages, each separated by 60 electrical degrees. This control is based on the motor's position. Normally, the motor position is obtained from three Hall Effect sensors. According, to the motor position the controller calculates the state in that the inverter must be such that the motor can produce torque. The Table 1 shows all the six states that can be observed.



**Figure 6 - Current path on a trapezoidal commutation [4]**

**Table 1 - Switching sequence for trapezoidal commutation**

Interval (degrees)	Motor Position			Inverter State			
	Hall A	Hall B	Hall C	ON Switches	Phase A	Phase B	Phase C
0 to 60	1	0	1	S1, S6	+	0	-
60 to 120	1	0	0	S3, S6	0	+	-
120 to 180	1	1	0	S3, S2	-	+	0
180 to 240	0	1	0	S5, S2	-	0	+
240 to 300	0	1	1	S5, S4	0	-	+
300 to 360	0	0	1	S1, S4	+	-	0

From the switching sequence results a current waveform that is trapezoidal. This commutation scheme is very simple and effective in controlling motor speed, but because this scheme only has six steps it tends to produce torque ripple depending on the actual motor BEMF.

### 2.2.1.2. Sinusoidal Commutation

By energizing all the three phases with sinusoidal currents (see Figure 7) it is possible to eliminate the plateaus shown in the trapezoidal commutation current waveform and replace them by waveforms that are sinusoidal. By having all the three phases energized continuously (see Table 2) a smoother torque is achieved and a more precise control can be reached. Usually, for minimal torque ripple and maximum efficiency the current waveform should match the BEMF waveform and be kept in phase with it.

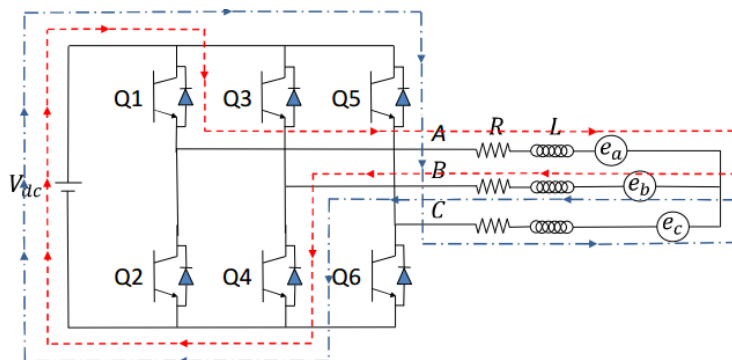


**Figure 7 - Current path on a sinusoidal commutation [4]**

**Table 2 - Switching sequence for sinusoidal commutation**

Interval (degrees)	Motor Position			Inverter State			
	Hall A	Hall B	Hall C	ON Switches	Phase A	Phase B	Phase C
0 to 60	1	0	1	S1, S6, S5	+	-	+
60 to 120	1	0	0	S1, S6, S2	+	-	-
120 to 180	1	1	0	S1, S3, S2	+	+	-
180 to 240	0	1	0	S4, S3, S2	-	+	-
240 to 300	0	1	1	S4, S3, S5	-	+	+
300 to 360	0	0	1	S4, S6, S5	-	-	+

The sinusoidal commutation requires high resolution position sensing, and the Hall effect sensors used in the trapezoidal commutation are usually replaced by an encoder. For this reason, the sinusoidal commutation is more expensive than the trapezoidal commutation but provides reduced torque ripple.

### 2.2.2. Phase Current Level Control

#### 2.2.2.1. PWM Current Control

PWM finds application in many fields, from the command of servo position to the transmission of digital data by a single signal in a serial protocol. In motors, PWM is a way of controlling the current level by turning the circuit on and off in pulses of different duration. Consider a load where the power supply is on during half of the time, in this case, the mean current level would be half the full power level. So, the current level is proportional to the turned-on time fraction.

When PWM is used in motors, the switching frequency is high enough such that the current ripple in the circuit is quite limited. The motor inductance limits the current gradient in time. So, what happens is that when the circuit is turned on: the current increases, when the circuit is turned off: the current decreases.

Typically, brushless motor controllers are based on PWM, relying on the inductance of the motor windings to smooth the current flow through the motor. If a purely resistive load has a PWM voltage waveform applied to it, the resulting current keeps the same waveform and is directly proportional to the instantaneous applied voltage, resulting in an unsmoothed pulsed current waveform - rippled current. The motor torque will be proportional to the mean current, but the motor Joule losses are proportional to the instantaneous current squared. Thus, the controllers depend on the inductance of a motor coils acting as filters for the resulting current, with a time constant of  $L/R$ . The rate of current variation in time is smaller in higher inductance circuit loads. since the current ripple degrades the motor efficiency, in a low inductance motor, higher switching frequencies are necessary to limit the current ripple to acceptable levels.

Using high PWM switching frequencies, an almost perfect sinusoidal AC can be modulated. In Figure 8, an analog circuit is presented that allows the creation of PWM AC. In this circuit, a comparator is fed with a reference sinusoidal wave signal,  $U_{rsw}$ , in the positive terminal that is compared with a triangular wave signal in the negative terminal,  $U_{tw}$ . When  $U_{rsw} - U_{tw} > 0 \Rightarrow S_A = 1$ , such that a pulse to the gates driver is generated. During the width of the pulse, the upper left gate and lower right gate close the circuit, applying  $+V_{DC}$  to the A phase motor terminal. During this condition,  $I_A$  increases in time with an increase rate proportional to the motor inductance. When  $U_{rsw} - U_{tw} < 0 \Rightarrow S_A = 0$ ,  $-V_{DC}$  is applied to the A phase motor terminal, making  $I_A$  decrease in time. Another possibility is a digital current controller based in sine function look up table for SA pulse width versus time determination.

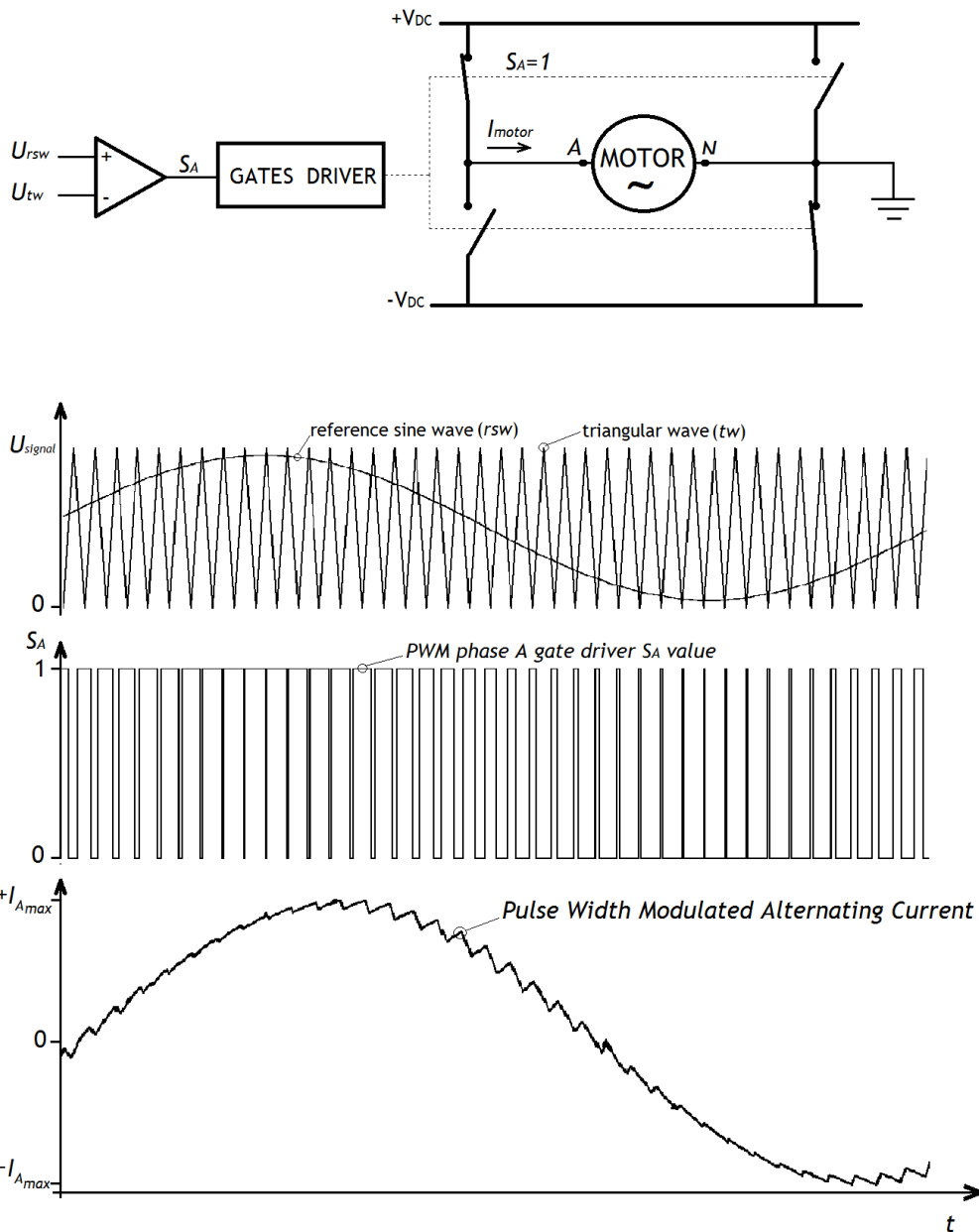


Figure 8 - Typical analog PWM Inverter

### 2.2.2.2. Hysteretic Phase Current Control

By using a hysteretic controller is it possible to shape the current waveform to any shape desired. In this method, each phase current is compared to a reference wave and switched in accordance with that. The switching signals are generated due to the error in the current waveform by comparing the reference current and the actual current (see Figure 9). If the actual current is higher than the upper limit of the hysteresis band the upper switch of the inverter should be turned off and the lower switch turned on such that the current falls. If, by the other hand, the actual current reaches the lower limit of the hysteresis band the lower switch of the inverter is turned off and the upper switch is turned on and the current starts to rise coming back to the hysteresis band. The band width is directly proportional to the current ripple and inversely proportional to the switching frequency.

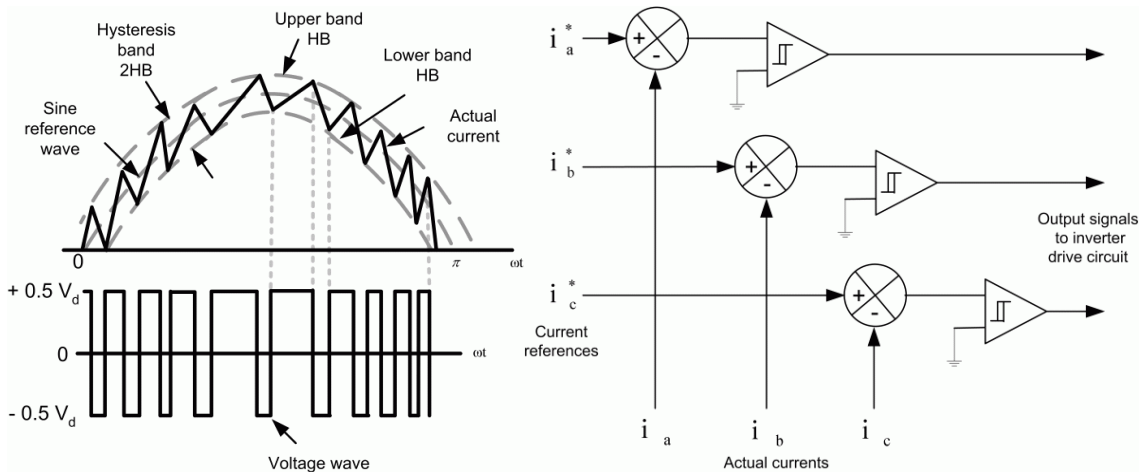
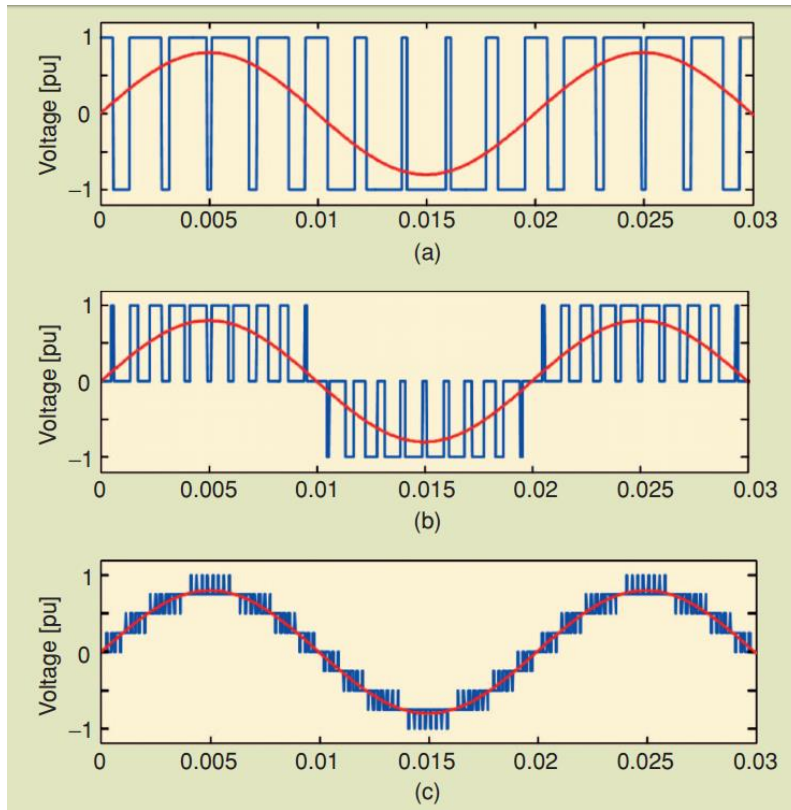


Figure 9 - Typical Hysteresis Current Controller [5]

### 2.2.2.3. Multilevel Inverter for Phase Current Control

A modern trend in inverters are the Multilevel topology inverters where  $n$  voltage levels are used to synthesize a sinusoidal voltage from a DC. Compared with the two-level inverter the multilevel inverter improves the output voltage quality, as shown in Figure 10 where is visible the improvement of the output voltage quality from a two-level inverter, in Figure 10 a), to a nine-level inverter on in Figure 10 c).



**Figure 10 - Multilevel Inverter Output [6]** a) two-level inverter, b) three-level inverter and c) nine-level inverter.

There are several topologies of multilevel inverters available and the differences are related to the switching mechanism and the source of the input voltage. Rodríguez et al [7] present a summary of multilevel inverter circuit topologies and their control strategies as well as their evolution.

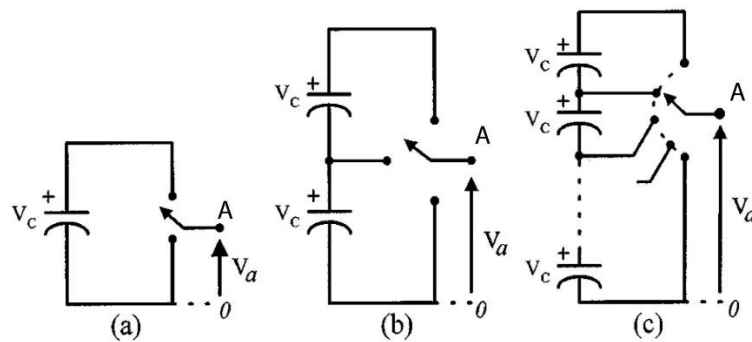


**Figure 11 - Multilevel inverter representation with: two levels a), three levels b), and n levels c)[7]**

The circuit of three-level inverters is shown in Figure 12. The inverter in a) provides a three-level output across phase terminal A. In the basic circuit, a three-position switch selects the voltage level for the phase terminal A. Unfortunately, such three-position switch does not exist

in discrete electronic components. So, to actually implement such circuit, there are a few options: Figure 12 b) shows the diode clamped topology and c) is the flying capacitor version of circuit a). In the diode clamped version, A can be at +VDC if switches  $S_1$  and  $S_2$  are on.  $S_1$  and  $S_2$  are complementary to  $S_1'$  and  $S_2'$ , respectively. So, they are off in such condition. A is at zero voltage level if  $S_2$  and  $S_1'$  are on. A is at -VDC if  $S_1'$  and  $S_2'$  are on. In the Flying capacitor topology, independent capacitors clamp the device voltage to one capacitor voltage level. In this case,  $S_1$  and  $S_2$  are not complimentary to  $S_1'$  and  $S_2'$ . To set the A terminal voltage level at +VDC, only switches  $S_1$  and  $S_2$  are on; if only switches  $S_1'$  and  $S_2'$  are on, A is at -VDC; to set A at zero voltage, only  $S_1$  and  $S_1'$  are turned on, making the capacitor  $C_1$  charge while trying to keep the 0 voltage or if  $C_1$  is charged, only  $S_2$  and  $S_2'$  are on to allow  $C_1$  to discharge while trying to keep the zero-voltage level. So, the charge of  $C_1$  is managed by the selection of the  $S_1$ ,  $S_1'$  or  $S_2$ ,  $S_2'$  switch combination. If the neutral terminal, in a single-phase motor had a similar three-level inverter, the three-level inverter would become a five-level inverter.

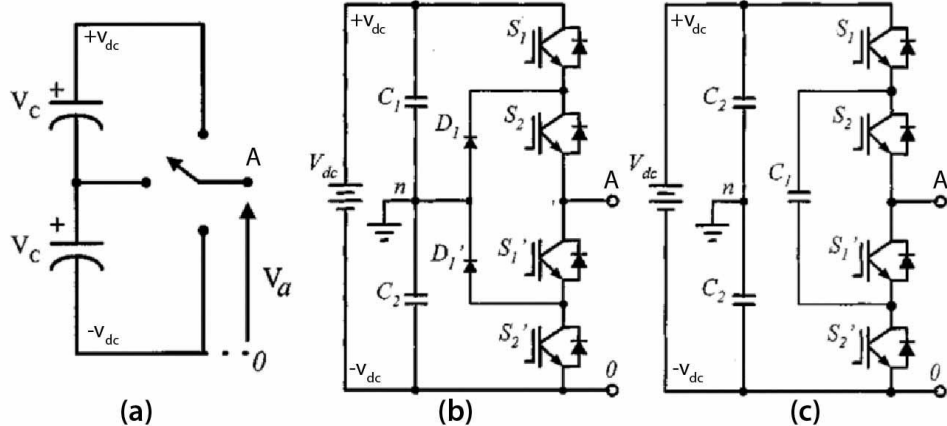


Figure 12 - Three-level inverter: a) basic circuit; b) implemented in a diode clamped topology; c) implemented in a flying capacitor topology adapted from [7]

The advantage of multi-level inverter becomes obvious when the load has low inductance and resistance, as in the case of a very efficient (low phase resistance) coreless (low inductance) motor. Specially, when the main factor opposing to the load current demand is the BEMF that changes with the motor speed, *i.e.*, with the vehicle velocity. Figure 13 shows the circuit of a single-phase load, five-level inverter with the Cascaded Multilevel inverter topology. It is based on single-phase full-bridge inverters connected in series with two separate DC sources. The resulting voltage level at the terminal A is synthesized by the addition of the voltages generated by the different levels [7].

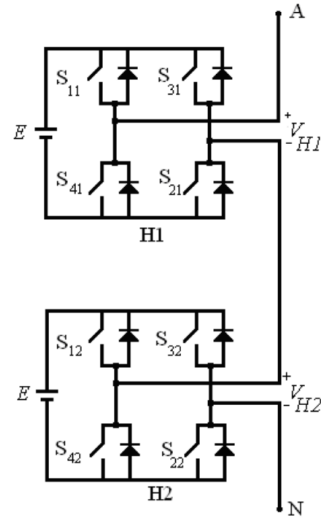


Figure 13 - Castaded half-bridge inverter [7]

#### 2.2.2.4. Field Oriented Control

Field Oriented Control (FOC) is an advanced control technique to drive electric motors that controls the stator currents by a space vector formulation to synchronize the phase current level with the phase BEMF. By knowing the exact position of the rotor, the controller calculates the inverter state to ensure that the stator field will be exactly 90 electrical degrees behind the rotor field (see Figure 14).

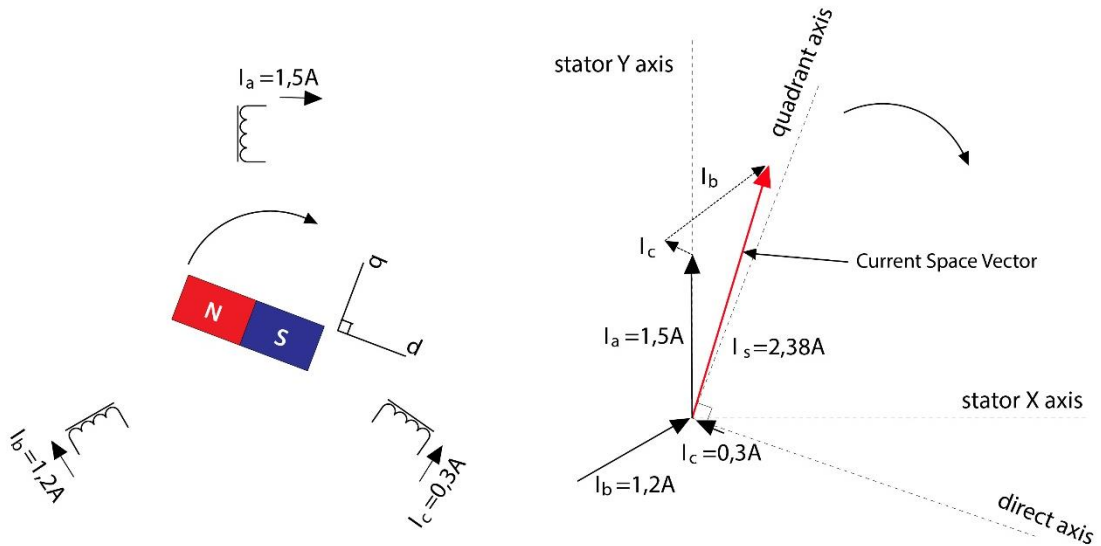


Figure 14 - Field Oriented Control Implementation [8]

FOC sees the three-phase stator currents (see Figure 14) as a flux and a torque components and controls both quantities separately. Through the Clarke's transformation the three-phase

sinusoidal currents ( $I_A$ ,  $I_B$ ,  $I_C$ ) are transformed into a two-phase time variant system ( $\alpha$ ,  $\beta$ ) that depends of the rotor frequency. Next, by using the Park's transformation, it is possible transform  $\alpha$  and  $\beta$  into a two-coordinate time invariant system ( $d$ ,  $q$ ) that is constant at a given rotor frequency. Where  $d$ -axis represents the flux, that is a function of the rotor position, and the  $q$ -axis represents the torque, that is a function of current. Depending of the input (desired torque), the control process redefines a new  $q$  quantity and adjust the  $d$  quantity in order to have  $d$  and  $q$  90 degrees apart. Through the inverse Park transformation, the new quantities of  $\alpha$  and  $\beta$  are calculated and translated back to the three-phase sinusoidal. Figure 15 shows a summary implementation of the FOC.

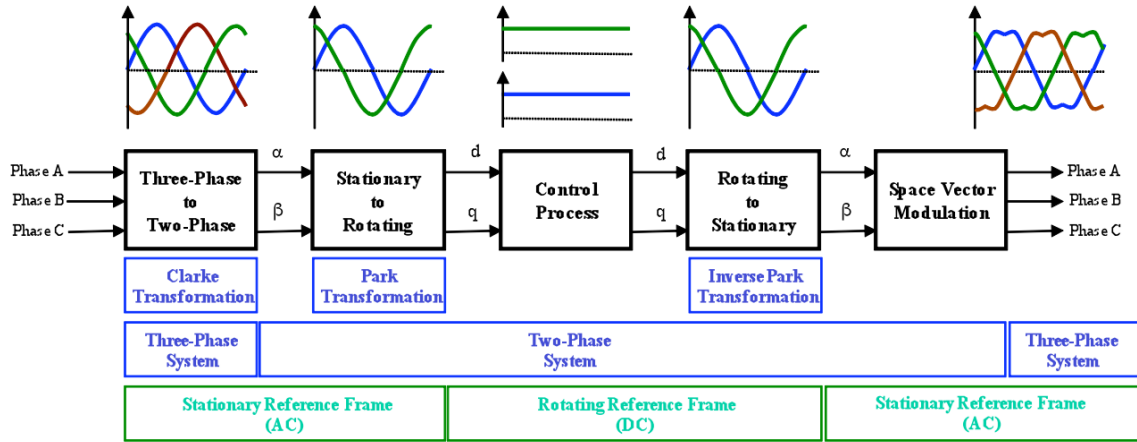


Figure 15 -Field Oriented Control Implementation [9]

## 2.3. State of the Art

In these section the latest efforts regarding motors and controllers that relate directly to the current work are highlighted.

### 2.3.1. PMSM Electrical Machines

Considering the presented PMSM fundamentals, the design concept for our motor is the three-phase axial flux coreless machine. The current state of the art review is, thus focused in this configuration. The works that present the actual efficiency of the motors or equivalent generators were favored. In reality, as explained in Section 2.2 the actual efficiency of the PMSM that must run from a DC bus supply can only be adequately measured if the motor is working in the generator mode or if it is run with a perfect controller.

Caricchi *et al* [10] describe the design, construction and experimental testing of an electric propulsion system to use in a dual-power city car based in an in-wheel three-phase coreless PMSM. A water-cooled axial-flux twin configuration for direct drive was developed. The twin motor configuration allowed the use of series to parallel motor connections adapting the system to vehicle speed and torque requirements. The efficiency curve with rotation speed was

remarkably flat near a maximum of 97%. Contributing to this performance was the controller that was part of the same development effort.

A solar vehicle in-wheel three-phase coreless PMSM was developed by CSIRO [11]. The motor uses an axial flux pancake configuration (see Figure 16). A Hallback magnet array was used to maximize the motor torque constant. Litz wire was used to minimize the induced current losses in the copper. The parametric study concerning the design is presented together with the design point performance. The final design weights 6 kg with 4.8 kg of rare earth Neodymium magnets, reaching an estimated efficiency is 97.8 %, the motor power is 1800W at 1060 rpm. This motor has been made commercially available as a kit by Marant [12] for around 10000 euros. A variant with a simple magnet array is also available at a lower cost but lower peak efficiency. These two versions are being used by various solar vehicle teams all over the world. Due to the low time constant, the high-end controller Titrium is used but still with 100  $\mu$ H inductors in series with the motor phases. The CSIRO motor is too powerful for a SEM prototype vehicle.

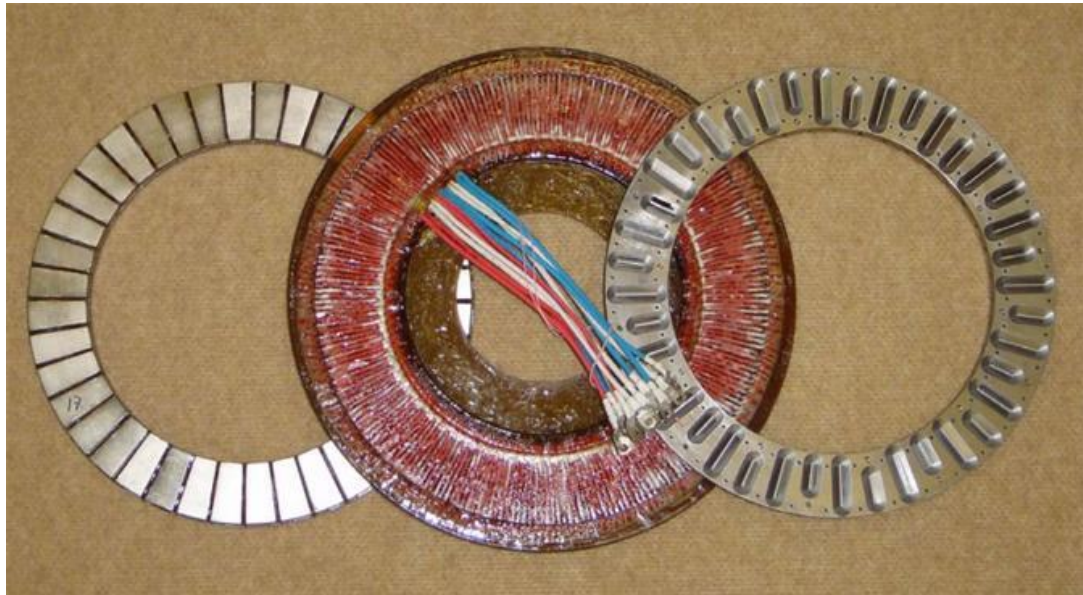


Figure 16 - Motor CSIRO [12]

Wang et al [13] described a method to calculate the performance of a coreless stator axial flux permanent-magnet (AFPM) generator. By combining the finite-element analysis and a theoretical analysis a multidimensional optimization methodology was created to optimize the design of AFPM generator. The results shown that the performance of the manufactured prototype is consistent with the predicted results.

Colton [1] presents in its MsC thesis, simple, low-cost design and prototyping methods for custom brushless permanent magnet synchronous motors. Different modulation strategies are explored to design the motors prototypes. He shows that using a first-order motor model analysis can predict the motor's performance with good accuracy. Three case-study motors

were used to develop, illustrate and validate the rapid prototyping methods for brushless motors, proving that these are useful in the fabrication of case study motors. One of the three case study developed motors was an axial flux coreless PMSM that showed a disappointing efficiency. This was attributed to not having considered the induced current losses in the copper of this coreless motor. Therefore, not having used Litz wire for that motor.

LaunchPoint Technologies, Inc in September of 2009 [14] presented a high efficiency brushless motor. Figure 17 shows the LaunchPoint's Electric Motor, it is axial flux with a dual permanent magnet Halbach array, also have an ironless rotor and stator to eliminate the eddy currents and hysteresis losses and an efficiency of 95%. This motor has the higher power density on the market, with 7 horsepower at 8400 rpm and 0,65 Kg of weight, it produces 11 horsepower per kilogram.

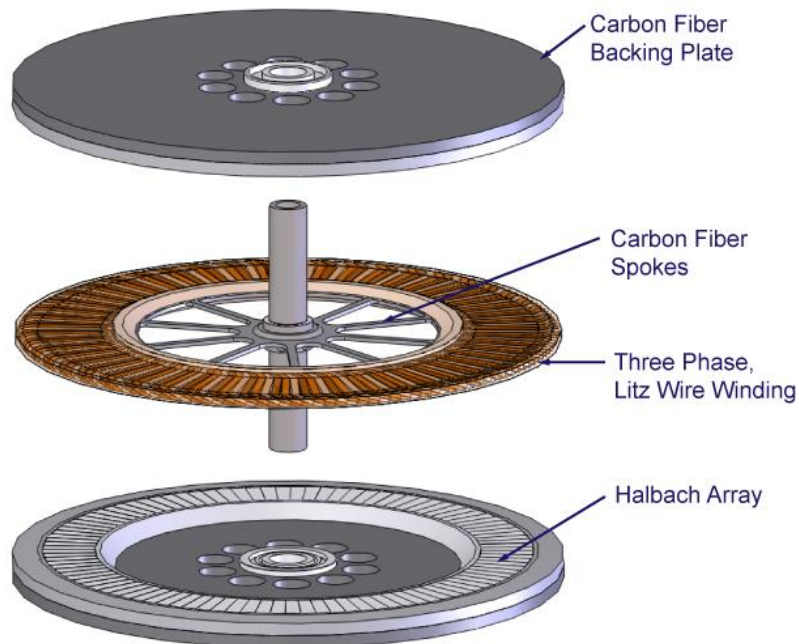


Figure 17 - LaunchPoint's Electric Motor [14]

Students from the Norwegian University of Science and Technology have been working on Axial Flux PMSM for their participations in Shell Eco-marathon. Their work was based on Lubna Nasrin design and the fabrication of the motor was described by Dahl-Jacobsen but the real performance of the motor wasn't the expected, so in 2012, Endresen [15] reports another build version of the Lubna Nasrin motor [16] where with changes in the motor windings and with a new arrangement of the magnets from a conventional North-South to a Halbach array, they believed that the motor would achieve 97,2% efficiency, with a mass of 6,24 kg. However, this improved version was measured reaching an efficiency of only 68%. This disappointing value was attributed to the difficulties found in the production of the rotor and the wiring. In 2013,

Buøy [17] built another version of the motor based in the Nasrin design but using different production methods.

Batzel et al [18] starting from requirements and drive constraints, such as power, speed, voltage and diameter designed and test an ironless axial-flux PMSM. A Halbach array was used to concentrate the magnetic flux on the air gap and allowing the absence of the backiron and reducing the weight of the motor. The machine efficiency was determined by measuring de phase voltages and currents - input and measuring the torque and speed of the shaft - output. The total weight of the motor was 4.8 kg and an efficiency over 90% was reached across the range of his operation.

Piggott developed a successful coreless permanent magnet, PM, generator for small-scale wind turbines. His design found widespread use since his designs and build instructions are published on various e-books and the vast majority are free to download. Beside the e-books, Piggott gives workshops around the world training the average person to build his generators. One of his first designs from 1993 was a PMG made by using a brakedrum from a Ford Transit. He built a three-phase radial-flux with ten coils per phase with a laminated core from an old electric motor [19]. In 2001 a new generator was published and it consists in machine that is a three-phase axial-flux with pancake configuration and four pole pairs mounted on each rotor disk and two concentrated coils per phase that are embedded in a polyester resin stator reinforced with fiberglass mat [20]. The rotor disks are made from car breaking disks and the magnets are regular grade 3 ferrite magnet blocks. In 2003 a new design plans were launched and some modifications to the configuration were made it became a 12 pole pairs 10 coils with five-phases [21]. The efficiency is not reported, but it is considered significantly better than the commercial ones.

Bumby et al described the design, construction and testing of two PMG for use in small scale wind turbines, one with 1kW of rated power and the other with 2,5kW, both generators were three-phase and had a pancake configuration with eight pole pairs and 4 coils per phase. They end up with a generator that is 93-94% efficient. They only had a maximum difference of 5% between the predicted and measured performance [22].

### **2.3.2. Motor Controller**

The development of motor controllers and inverters has been extensive in later years. This is due to the expansion of grid tied solar roofs in the case of inverters and due to the advent of electric plug-in cars. Motor controllers and inverters are very similar. Only the works that inspired the adopted controller solution are referend herein.

Due to the very low inductance that coreless PMSM are characterized, Caricchi *et al* [10] implemented a current ripple reduction by adjusting the voltage supplied to the motor

controller in accordance with the motor's EMF using a dc-to-dc buck-boost converter. Figure 18 represents the layout of the motor drive control system presented.

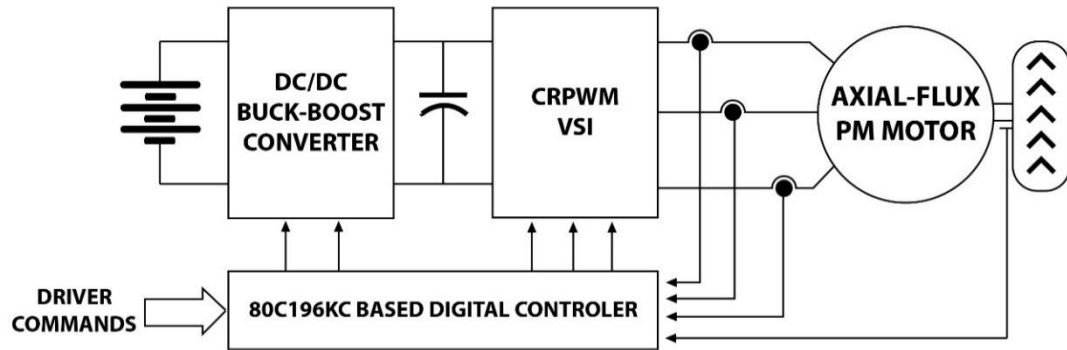


Figure 18 - Layout of the motor drive control system presented by Caricchi et al [10]

Colton [1] also, in his MsC thesis developed, built and tested a brushless motor controller with two channels and 1kW per channel. Great efforts were made to implement FOC on low-cost hardware. The electrical requirements for the controller and selection of the main components also were discussed in his report.

Bossche et al [23] developed a three-phase BLDC motor controller to fit in a small Electrical Vehicle. This controller is based in a Programmable Logic Device, they realize that for their controller only use combinatory task, such as AND, OR, Enable and with some additional analog and digital electronics they don't need a complex microcontroller. They implemented a very simple torque control where the current supplied to de motor is measured in two phases and the third is analogical calculated.



# Chapter 3

## 3. Methodology

In the present chapter reports the development of both: motor and controller.

### 3.1. Motor Development

This first section describes the efforts to develop the SEM car prototype motor. The implemented concepts in the motor are described in the conceptual design (Section 3.1.1), then a preliminary design was computed embodying all the concepts. Finally, a detailed design was created in CATIA 3DCAD software supported by performance calculations in the form of parametric studies. Finally, a prototype was built and tested.

#### 3.1.1. Conceptual Design

To design and build a motor, important decisions must be made in the conceptual design phase having in consideration: the different types of motors, the availability of different materials, the access to fabrication machinery and the total cost of the motor. It is very important to match the motor typology to its function and to respect the current objective of obtaining an ultra-efficient motor.

In electric vehicle applications, the use of a direct-drive motor is desirable because of the elimination of the reduction and transmission losses. At the same time, results in low vehicle cost and system volume, higher reliability and an increase of the total vehicle efficiency. In consideration of the high-torque operation required at relatively low speeds, permanent magnet (PM) motors are best fit to the direct-drive application [24]. So, from the beginning of this project one choice was made, an in-wheel direct drive motor will be used. In this motor, electronic commutation can be used in lieu of mechanical brushes, although the electronic commutation complexity, the efficiency and reliability favors this type of motor in our application. It was decided to develop the motor from the concept previously used with success in solar electric car competitions, the CSIRO motor [11]. It is an axial flux permanent magnet coreless synchronous motor. One important requirement is, thus, that the motor should fit inside the wheel, reducing the aerodynamic drag and maximizing the efficiency. Such type of motor has low inductance,  $L$ , because it has no iron core in its coils, and at the same time, it must have the lowest possible resistance,  $R$ , because the Joule losses are directly proportional to the resistance. It is, thus, characterized by very high phase current gradients while despite the efforts to reach a low  $R$ , the time constant  $L/R$  will remain extremely low. Therefore, this type of motor it is prone to very large current ripple. This is the reason why it was decided that

the motor and controller should be developed in a single work package. The efficiency of the motor running in the vehicle depends from the controller performance.

In the conception of the Aero@UBI01 car, in the initial stage, a model to predict the car performance was developed with the most significant parameters regarding to the car performance, with this model the motor power requirements were determined.

SEM race rules dictate that the prototype category vehicles must perform with a mean speed of 25 km/h for the race (7.03m/s). In our case, it was realized that, in the same way the electric current ripple increases the Joule energy losses in the motor for the same mean current value, an airspeed ripple during the race increases the drag losses for the same mean value of 25 km/h. So, considering the absence of atmospheric wind during the race and that the race track in Rotterdam, Netherland, is mostly flat, it was decided that the driver must maintain the 25 km/h and, thus, the motor is designed for maximum efficiency at that continuous power and torque design point condition with the possibility of having moments during the race where higher power or torque is needed. *E.g.*, overtaking another vehicle in the racing circuit. Considering the wheel diameter of 0.478m, the angular speed of the motor will be 29.4 rad/s.

Regarding the motor efficiency goal, the parametric study of the car prototype performance indicated that the motor could be made 3kg heavier if the efficiency would rise 1%.

**Table 3 - Motor requirements**

Requirement	Value
Continuous output shaft power (cruise)	15W
Peak shaft power (climb)	400W
Rotational speed at 25.1km/h (7,03m/s)	29.4 rad/s
Continuous Torque (cruise)	0.510Nm
Peak torque (climb)	13.605Nm
Maximum Outside diameter	370mm
Maximum Axial Length	70mm

The conceptual design of the motor results from the implementation of multiple ideas and concepts. Here is a list of the other implemented concepts:

- **PMSM** - is the motor type that achieves the highest efficiency as explained in Chapter 2. So, the intent was to pursue a PMSM machine driven by a close to sinusoidal current;
- **In-wheel direct drive**- for the nonexistent transmission losses and motor bearings losses and no volume is required inside the vehicle for transmission and the motor itself;
- **Axial flux rotor configuration** - is suitable to fit in the vehicle's wheel (see Figure 22);
- **Coreless** - the iron laminate core of most PMSM is responsible for Eddy current losses and magnetization hysteresis losses. One drawback of the coreless motor concept is that Eddy current losses occur in the stator copper windings but can be prevented by

the use of suitable Litz wire [11]. Another drawback is that the magnet flux is not forced into the coil dispersing at a short distance from the magnets faces. So, thin stator coils that are very close to the magnet face are required;

- **Steel back rotors** - the magnetic flux between rotor magnets is closed by ferromagnetic steel plates that act also as a structural rotor support to hold the magnets;
- **Litz wire use** - to minimize Eddy current losses occurring in the stator copper, the use of Litz wire was mandatory. The copper wire Eddy current losses are proportional to the fourth power of the wire diameter [13]. From the search for a Litz cable provider, the commercially available specifications and the stator geometry and dimensions led to the choice of the 10x18 individually insulated wires of 0.1mm diameter;
- **Configurable motor** - the use of a single wave winding turn from a cable of 10 sets of 18 individually insulated wires allows to configure the motor winding with multiple winding options. From the basic configuration of a single turn with 180 parallel wires to a 10 turn coil of 18 parallel wires. In this manner, the motor constant is, in fact, adjustable to a different application of the motor;
- **Three-phase** - because it is the minimum phase number allowing constant torque which is crucial when starting the vehicle;
- **Minimized stator thickness between opposing magnet poles faces** - due to the coreless concept magnet flux dispersion, the thinner the stator the better. This was achieved by adopting wave winding and using a single turn per phase for the motor. So, the motor stator is as thin as a single squeezed cable of 10x18 isolated wires (~3mm). The three phases do not overlap in the stator between the magnets, they overlap in the radial inner and outer edges of the stator, outside the inter faces region existing between opposing magnets;
- **Wave winding** - wave winding was adopted because allows the smaller stator thickness (see Figure 19);
- **Special end-turns inter-phases overlapping** - the overlapping of the phases windings is limited to radial inner and outer edges of the stator, contrary to the CSIRO in-wheel motor where they overlap in between the opposing magnets faces [11];
- **N52 NdFeB magnets** - rare earth magnets are becoming standard in PM motors. They allow greater magnetic flux in the stator coils per magnet unit mass. Thus, reducing the coils turns therefore the length of coil wire, therefore smaller phase resistance, size and weight to reach a given motor constant,  $K_t$ , and efficiency. The drawback of these higher specification limit magnets is the operating temperature limit (80°C). But, for a high efficiency and small power motor with little restrictions in size and weight, the temperature builds up in the motor is not an issue;
- **Low cost magnets per unit mass** - the mass of magnets relates inversely with the size of required coils to reach a given motor constant,  $K_t$ , and efficiency. So, to make use of the least cost restricted mass of magnets possible, the commercially available NdFeB magnets with lowest price per unit mass were identified. For the small number of

magnets necessary for the motor prototype, the minimum price that was found was 51€/kg. Given all the geometrical constrains and number of pole pairs optimization, the chosen magnets were at a price tag of 60€/kg;

- **Gap between magnets** - the placement of magnets was such that there was a gap between them approximately equal to the magnet thickness because it was believed that such arrangement would result in a BEMF closer to sinusoidal.
- **Adjustable air gap** - although the air gap is, generally, minimized, the option to make it adjustable allows to fine tune the motor constant to the actual motor use.

The final conceptual design of the developed motor is shown in Figure 20, Figure 21 and Figure 22.

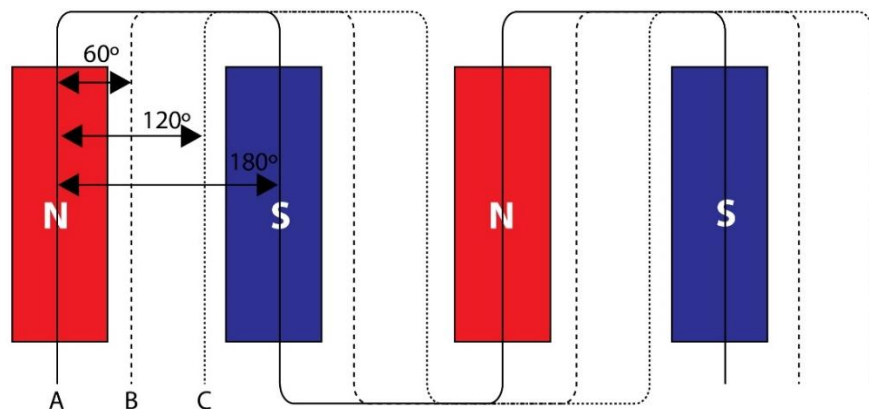


Figure 19 - Wave winding concept

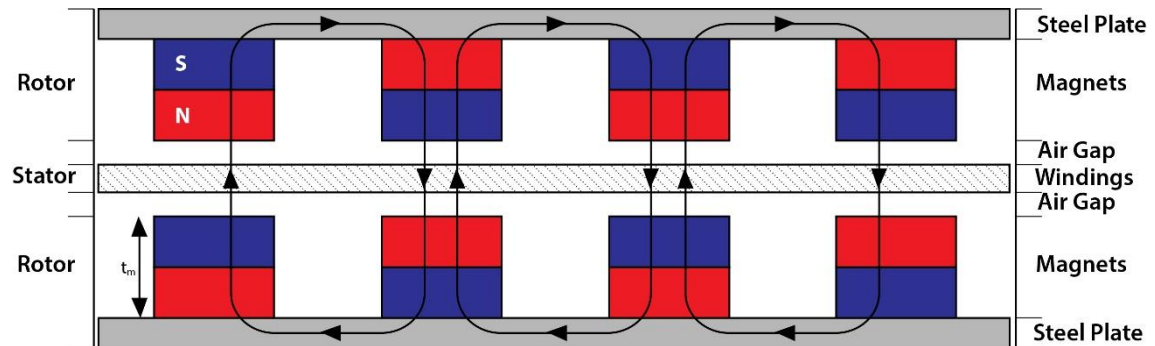


Figure 20 - Motor axial flux coreless motor concept

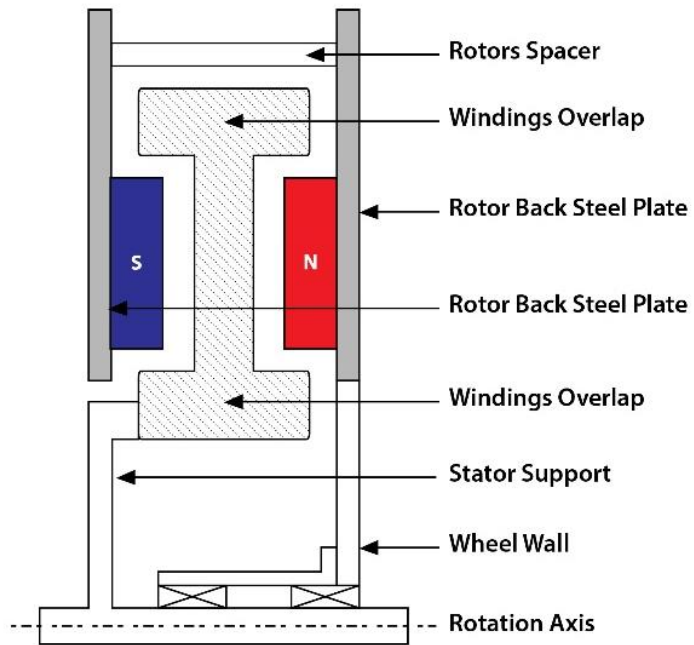


Figure 21 - Motor section concept

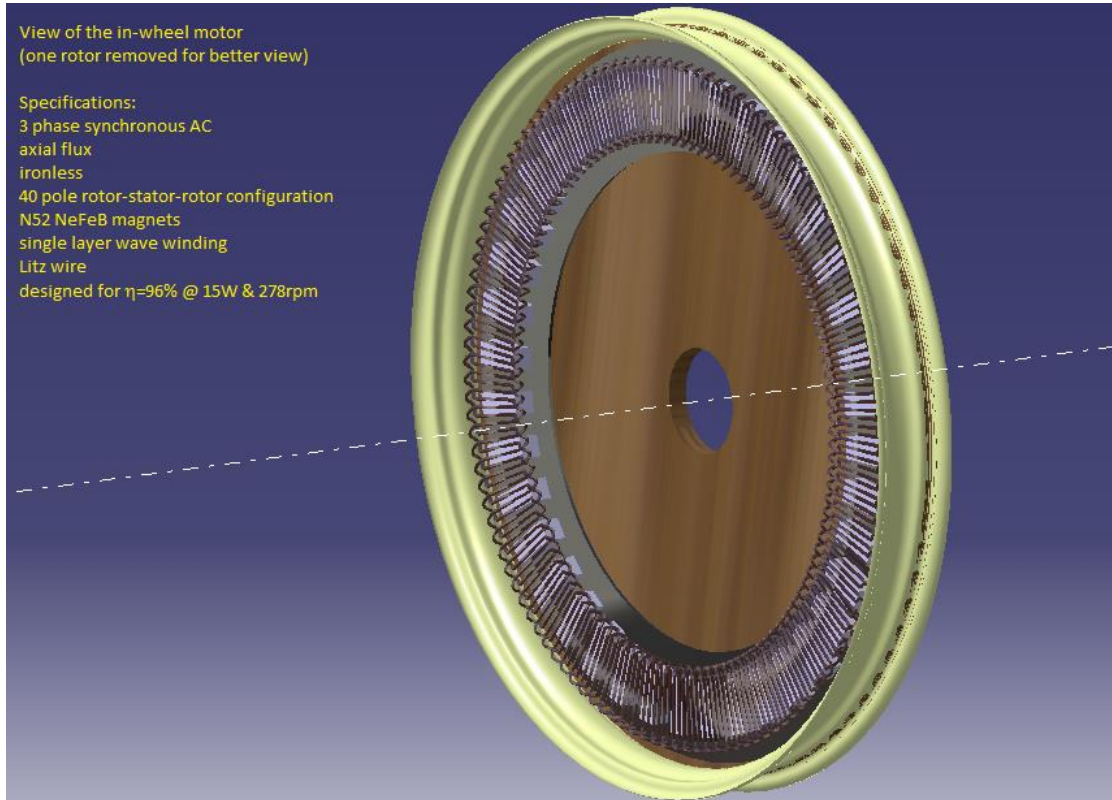


Figure 22 - First motor concept design.

### 3.1.2.Preliminary Design

The motor design variables were: Voltage of the DC bus,  $U_{DC}$ ; Shaft Power,  $P_c$ ; angular speed,  $\omega$ ; Motor Efficiency,  $\eta_c$ ; mean radius at magnets center position,  $r$ ; magnet poles number,  $p$ ; flux intensity of the magnets,  $B_{mag}$ ; magnet thickness  $tm$ , Stator filling factor,  $FF$ ; magnet pole length,  $L$ ; magnet pole width,  $W$  and the airgap thickness of 2mm. So, in the first design iteration, all these variables values were assigned.

In the case of  $U_{DC}$ , it had to be a multiple of 3.7V because the SEM competition rules mandate the use of a lithium-ion battery. In the first design iteration, the value was set to 7.4V but the final design point uses 15V and the actual vehicle's battery uses 22.2V to reach a top speed sufficiently above the design speed. Table 3 shows the values that were used for  $P_c$ , 15W, for  $\omega$ , 29.4rad/s and the maximum radius of the motor,  $340\text{mm}/2=0.17\text{m}$ .

The main constrain for the motor development was the motor cost and he main cost share was found to be for the magnets. So, these were chosen for their low cost; their geometric suitability to the in-wheel motor, and peak magnetic flux density rating. The adopted magnets were N52 flux rated NdFeB magnets with  $L=0.030\text{m}$ ;  $W=0.012$  and  $tm=0.012\text{ m}$  costing 60€/kg. So, the mean radius of the magnets was set at 0.15m ( $0.17-0.03/2=0.155$  subtracted of a 5mm radial margin). The magnetic flux density of these N52 specified magnets reaches a  $B_{mag}=1.48\text{T}$ . A stator filling factor of  $FF =0.3$  was assumed. The major unknowns were the number of magnet poles and the efficiency that the motor could be designed for. So, during the design iterations,  $p$  was varied in the range of 32 to 40 and  $\eta_c$  from 0.96 to 0.99.

To model the motor, the first step is to obtain the available AC tension,  $U_{AB_{rms}}$  from the U (1).

$$U_{AB_{rms}} = \frac{\sqrt{3}}{2\sqrt{2}} U \quad (1)$$

The motor electrical power is obtained from the shaft power, using the design point motor efficiency (2).

$$P_e = \frac{P_c}{\eta_c} \quad (2)$$

From the motor electrical power, the motor current is obtained (3).

$$I_{rms} = \frac{P_e}{U} \quad (3)$$

The motor phase current is also obtained from the motor electrical power, (4).

$$I_{ABC\ rms} = \frac{1}{\sqrt{3}} \frac{P_{ce}}{U_{ABrms}} \quad (4)$$

Knowing motor phase current, the motor total Joule power loss is calculated with Equation (5) assuming half the losses will occur due to internal flow drag (windage loss) and eddy-currents in the copper. So, the windage power loss is equal to the Joule power loss.

$$3RI^2 = \frac{(P_{ce} - P_c)}{2} \quad (5)$$

The phase winding resistance is found from the total Joule power loss by Equation (6).

$$R = \frac{RI^2}{3I_{ABCrms}} \quad (6)$$

The motor resistance voltage drop, which is the required electromotive force to reach the motor phase current is calculated from Equation (7).

$$U_{emf} = 3RI_{ABCrms} \quad (7)$$

The required motor effective back electromotive force,  $U_{bemfrms}$ , is obtained from Equation (8).

$$U_{bemfrms} = U - U_{emf} \quad (8)$$

The motor constant  $K_t$  is now obtained from Equation (9).

$$K_t = \frac{U_{bemfrms}}{\omega} \quad (9)$$

The angle corresponding to half electric revolution is calculated from the motor pole pair number  $p$  from Equation (10).

$$\alpha = \frac{2\pi}{p} \quad (10)$$

The duration of the coil motion from one magnet to the next is calculated from Equation (11).

$$t_{mag} = \frac{\alpha}{\omega} \quad (11)$$

The motor stator mean perimeter is given by Equation (12).

$$p_{er} = 2\pi r \quad (12)$$

The stator outer perimeter is given by Equation (13).

$$p_{er_{out}} = 2\pi r \left[ r + \frac{L}{2} + 0.005 \right] \quad (13)$$

The stator inner perimeter is given by Equation (14).

$$p_{er_{inn}} = 2\pi r \left[ r - \frac{L}{2} - 0.005 \right] \quad (14)$$

The distance between opposing magnets faces, for the air gap in each face of the stator plus the stator itself with thickness,  $t_s$ , (see Figure 20) is determined by Equation (15).

$$g = t_s + 4 \quad (15)$$

Regarding the mean flux density at the stator, it was considered to be 90% of the peak magnet flux density and proportional to the total thickness of the magnets surrounding the stator coil,  $2t$  (see Figure 20) is determined by Equation (16).

$$B_{coil} = 0.9B_{mag} \frac{2t}{(g + 2t)} \quad (16)$$

The wave winding coil area subjected to the magnetic flux is calculated according to Equation (17).

$$A = LWp \quad (17)$$

The magnetic flux is calculated from Equation (18).

$$\phi = AB \quad (18)$$

The pole width available at the mean stator perimeter is  $p_{er}/2$ . The desired magnet width was checked as  $p_{er}/4$ . It should be close to  $W$  such that the gap between successive rotor magnets was close to the value of  $W$ . It could never approach  $2W$  or the magnets could not be fitted in the rotor.

The flux gradient in the stator coil is considered as  $\frac{2\phi}{t_{mag}}$ . A maximum single coil voltage drop was calculated by Equation (19).

$$RI = 1.25RI_{ABC\ rms} \quad (19)$$

So, the required maximum phase voltage is given by Equation (20).

$$U_{ABC} = \frac{U_{AB\ rms}}{\sqrt{3}} - RI \quad (20)$$

The required turns per coil is obtained from Equation (21). The actual design point had to correspond to a finite  $N$  number.

$$N = \frac{U_{ABC}}{\frac{2\phi}{t_{mag}}} \quad (21)$$

The length of coil wire per turn per coil is obtained from Equation (22).

$$lp = 2p(L + 0.01) + 0.6p_{er_{out}} + 0.6p_{er_{inn}} \quad (22)$$

The total wire length per coil is obtained from Equation (23).

$$l_N = N(lp + 1) \quad (23)$$

The minimum copper coil wire section area was calculated from Equation (24) considering a copper wire resistivity at 40°C of  $2.06 \times 10^{-8} \Omega \text{m}$ .

$$A_N = 2.06128 \times 10^{-8} \frac{l_N}{R} \quad (24)$$

The corresponding diameter was calculated from Equation (25).

$$d_{wire} = 2 \sqrt{\frac{A_N}{\pi}} \quad (25)$$

The minimum copper volume per phase was calculated from Equation (26).

$$V_{wire} = A_N l_N \quad (26)$$

The motor stator copper mass for the required copper volume per phase was calculated by Equation (27) considering a copper density of 8930kg/m<sup>3</sup>.

$$m_{wire} = 8930 V_{wire} \quad (27)$$

The stator disk area perpendicular to the axial axis was calculated from Equation (28).

$$A_S = 2\pi \left[ \left( r + \frac{L}{2} + 0,005 \right)^2 - \left( r - \frac{L}{2} + 0,005 \right)^2 \right] \quad (28)$$

The required stator thickness was calculated considering the filling factor from Equation (29).

$$t_s = \frac{3V_{wire}}{A_S F_F} \quad (29)$$

The required motor magnets mass was calculated, considering the filling factor from Equation (30) and considering a NdFeB magnet density of 7500kg/m<sup>3</sup>.

$$m_{mag} = 2p(7500WL t_m) \quad (30)$$

In order to decide what pole count, p, would be used in the motor, a parametric study was performed to see how much mass would the motor have due to the desired design efficiency. So, calculations were performed to determine the copper mass in the stator windings due to the adoption of different pole count in function of the design point efficiency of the motor. The study was performed in a range of 32 to 40 poles. The magnet mass for 32 poles was

estimated at 2.1 kg and for 40 poles a value of 2.6 kg was expected. The results are presented in Figure 23. The results for the total mass of rotor magnets plus stator copper are presented in Figure 24. The adopted design was considered a good compromise between magnet mass, the corresponding cost and the value of efficiency that corresponded. A higher magnet poles number would increase even further the total magnet mass and, thus, motor cost.

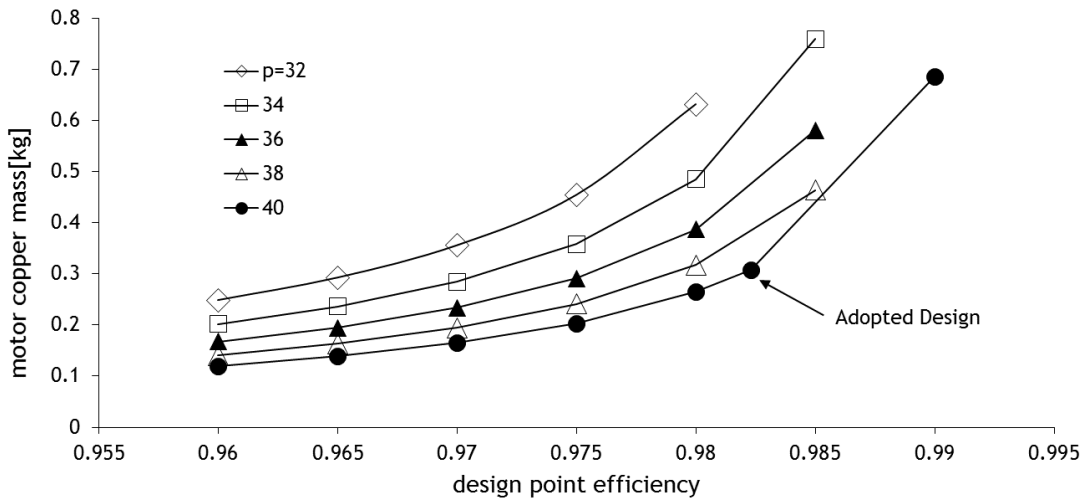


Figure 23 - Motor stator copper mass due to pole count in function of design point efficiency

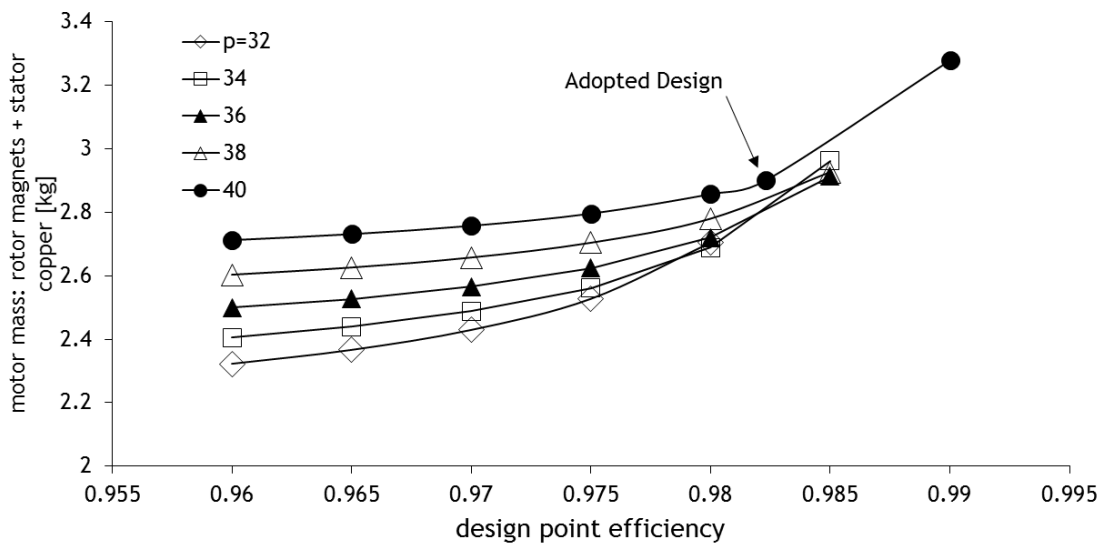


Figure 24 - Motor mass versus design point efficiency.

### 3.1.3. Detailed Design

From the preliminary design study presented in Section 3.1.2 and implemeting the concepts from the conceptual design (Section 3.1.1) the final design of motor was created in CATIA V5 CAD software. Table 4 shows the parameters of the adopteddesign.

Table 4 - Motor Parameters

Geometrical Parameters	Value
Outer dimameter	0,370m
Inner diamenter	0,260m
Axial length of the motor	0,070m
Radial lenght of the motor	0,370m
Radial lenght of the motor	0,195m
Number of turns	2
Fill factor	0,3
Torque constant	0,504 Nm/A
Air gap	0,007m

Electrical losses	Value
Nominal motor current	1,031 A
Resistance	0,048 Ω
Copper loss	0,066 W
Magnetic flux density	1,029 T
Windage loss	0,0676 W

Weight	Value
Magnet mass	2,59 Kg
Copper mass	0,31 Kg
Total weight (Magnets and Copper)	2,90 Kg

The motor design is based in the two principal parts of the motor: the rotors and the stator. The rotors plates are separated by 20 screws that resist to the magnentic attraction between the rotors magnets, this screws are also used to align the rotors in the assembly and dissasembly of the motor and to ajust the air gap. The stator is secured in position by three screws that allow adjustment of its plane in relation to the rotors in order to correct any misalignment if necessary. A CAD rendering of the motor in an exploded view is shown on Figure 25.

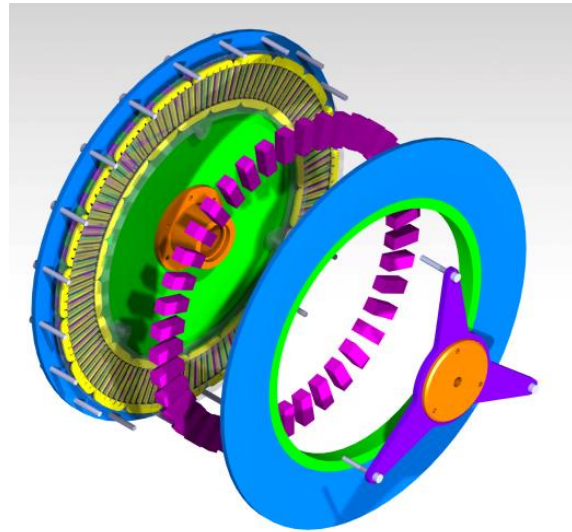


Figure 25 - Final motor design

### 3.1.4. Fabrication

Through the simplification of the motor design it was possible to fabricate most part of the motor's components in-house. The rotor back steel plate was only component that had to be manufactured outside.

#### 3.1.4.1. Stator

The stator of the motor is composed by an I profile shape (shown in Figure 21) in a circular solid revolution containing the three-phase windings. Figure 26 shows how the three-phase windings are distributed in space respecting the configuration shown in Figure 19.

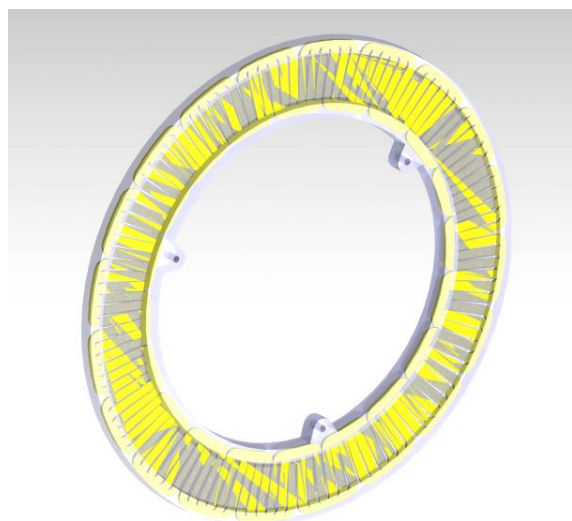


Figure 26 - Stator design

To make the desired stator shape, the selected manufacture process was resin casting. From the detailed design, a female mold with two parts corresponding to both faces of the stator was made from high density polyurethane foam (Sikablock®) using a three-axis Computer Numeric Control (CNC) router. In the fabricated mold, the position of the three-phase windings were marked (see Figure 27) and then the copper Litz wire was placed according to each phase winding position. Figure 28 shows the placing of the windings in the female mold before casting resin. The mold was then closed and filled with epoxy resin.

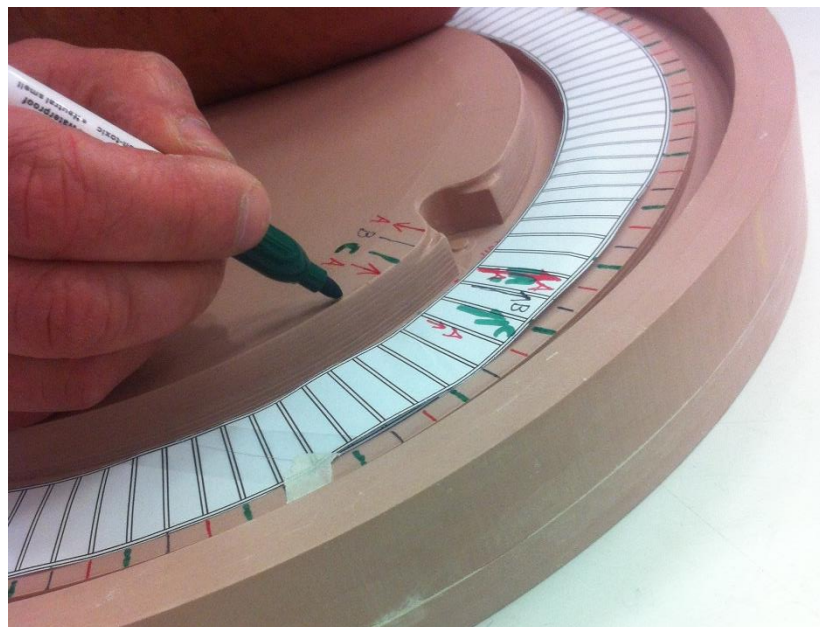


Figure 27 - Phase winding markings

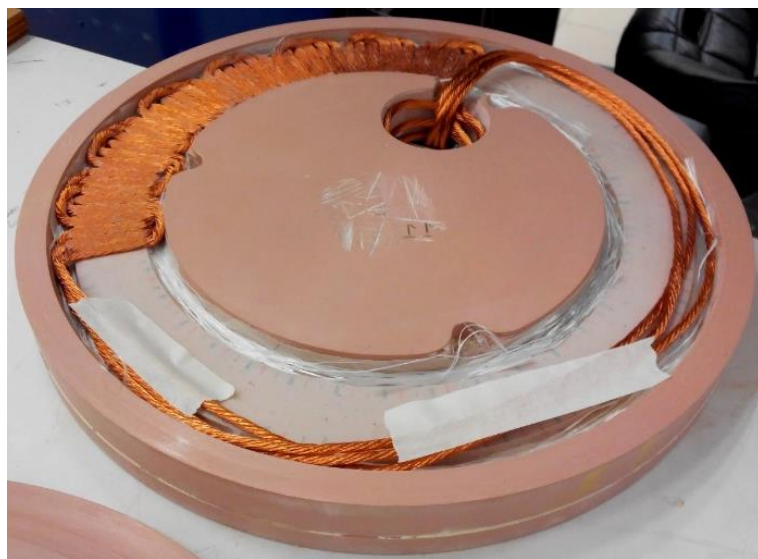


Figure 28 - Stator fabrication before pouring the epoxy resin.

### **3.1.4.2. Rotor Manufacture Process**

The rotor disks of the motor are based in two soft steel rings that were laser cut from a 5mm thickness plate. The 5mm thickness rings provide the magnetic flux between magnets without saturation (see Figure 21). They also have the stiffness to resist the magnetic force between rotors that can build up to an order of 10000N as they come close together. The total weight of both steel rings is about 4.3kg (it is definitely a mass to eliminate in a future version of the motor). A plywood rig (shown in Figure 29) for the magnets was glued with epoxy to precisely position the magnets. This plywood magnet placement rig ring was built by CNC machining it in the 3-axis router and became part of each rotor disk. In one of the rotors, this plywood rig is used as a structural support for the wheel wall that is also made of 6mm thickness plywood. This plywood wall is also supporting the rotor. One of the rotor disks is kept in place solely by the attraction to the other rotor disk that is supported by the wheel plywood wall (see Figure 21).

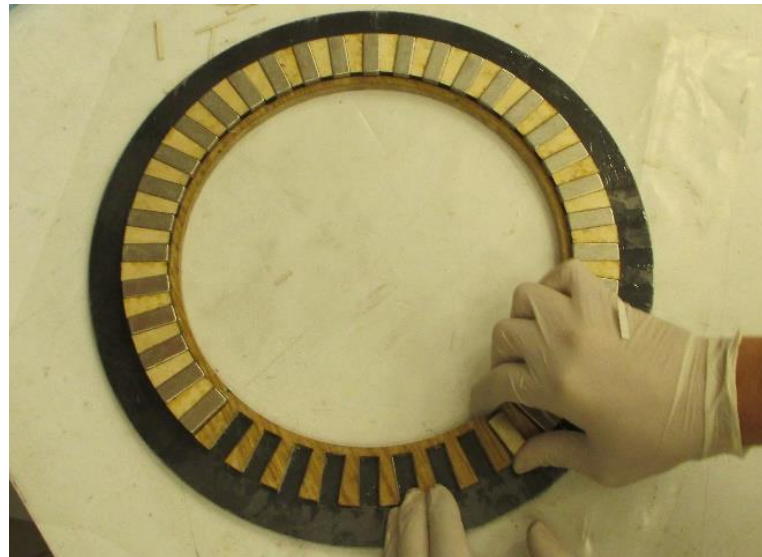


Figure 29 - Rotor fabrication - placing the magnets

### **3.1.4.3. Stator Support**

The torque of the motor acting on the stator is transmitted to the stationary part of the axle through a three-point star shape made of plywood with 5mm thickness (see Figure 30). The plywood was reinforced with 200g/m<sup>2</sup> glass fiber bidirectional weave in both faces in a sandwich configuration to increase its strength and stiffness.

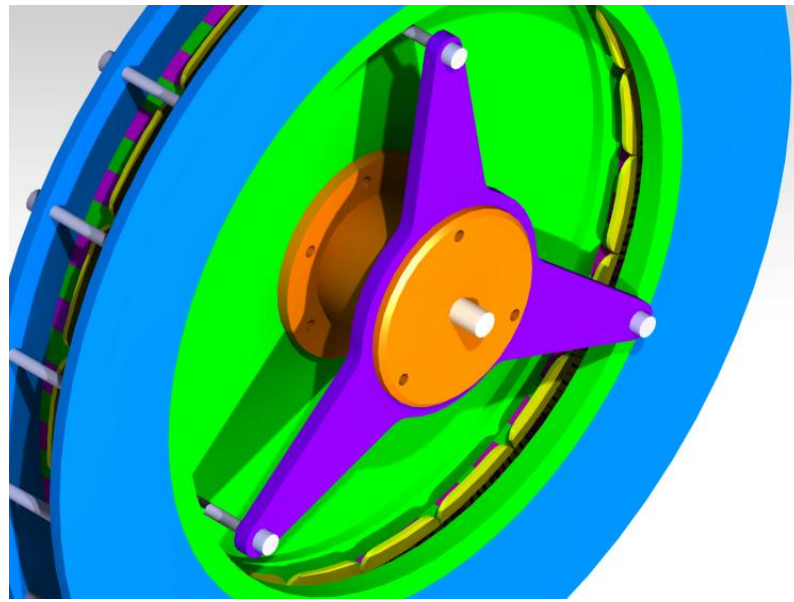


Figure 30 - Stator Support

#### 3.1.4.4. Wheel/Motor Hub

Because the designed motor is an in-wheel motor, the wheel and the motor share the hub. To be lightweighted, the wheel/motor hub was made from aluminum, on a lathe. Full ceramic bearings were used to minimize the bearing friction. The designed wheel/motor hub (painted in orange) and one of the ceramic bearings (painted in light blue) are shown in Figure 31.

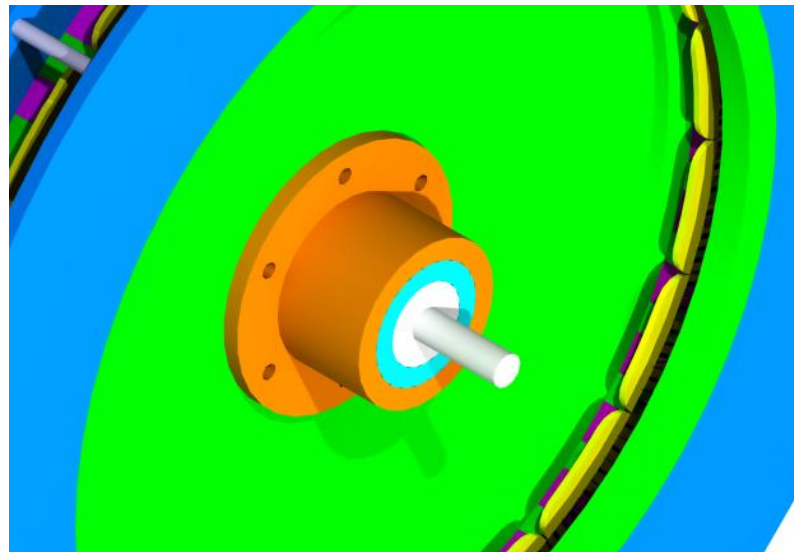


Figure 31 - Wheel/Motor Hub

### **3.1.5. Motor Testing**

After the fabrication of the motor, it was tested to compare its real performance against the calculated design.

#### **3.1.5.1. Back Electromotive Force**

One of the simplest tests that could be done to the motor was to measure the BEMF and compare with the predictions made in the detailed design. By comparing the predicted BEMF at the design point with the BEMF from the motor, it was possible to evaluate if the developed motor will behave like predicted. By measuring the two terminals of one phase with an oscilloscope it was possible observe the shape and amplitude of the BEMF while the motor was running powered by hand.

#### **3.1.5.2. Motor Mechanical Losses Measurements**

The measurement of the mechanical losses on the motor was done by measuring its kinetic energy drop per unit time when freewheeling near the design angular speed of 277 rpm. The experiment starts by accelerating the motor to about 285 rpm and measure the time it takes to decelerate to 270 rpm. Knowing the kinetic energy of the motor rotor at two different angular speeds and the time that it takes to deaccelerate between them, the total freewheeling power loss is determined.

To determine the kinetic energy at a given angular speed, the moment of inertia of the motor also had to be determined. So, it was measured too.

##### **3.1.5.2.1. Motor Rotor's Moment of Inertia Measurements**

Figure 32 shows the test rig used to measure the moment of inertia. Where the motor was mounted with the terminals of one phase connected to the oscilloscope to acquire its frequency (thus, angular speed). A falling mass,  $m$ , of known value was hanged by a cable wound in the periphery of the rotor to accelerate the motor during a known vertical distance drop. The final motor's angular speed was measured. Since the energy supplied by the falling mass is known, the motor rotor's moment of inertia is related to the measured motor angular speed by Equation (31). The results are presented in Section 4.1.2.

$$I = \frac{2 \left[ mgh - \frac{1}{2} m (\omega r)^2 \right]}{\omega^2} \quad (31)$$

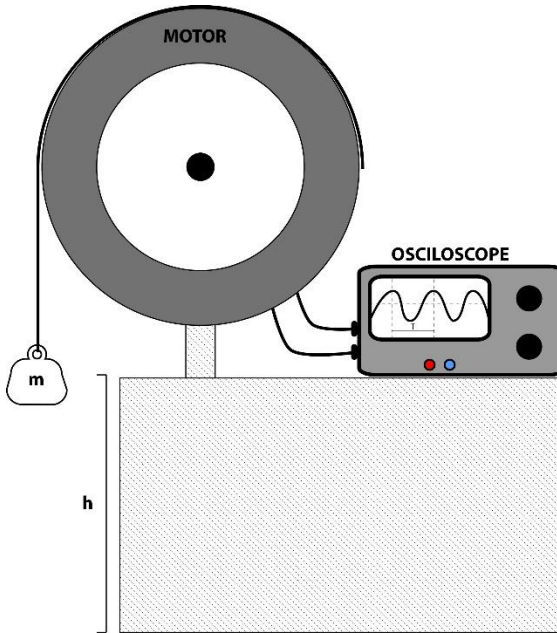


**Figure 32 - Moment of Inertia Measurement: Test rig schema to measure the motor rotor's moment of inertia.**

### 3.1.5.2.2. Mechanical Losses Measurement

To measure the time that it takes for the motor to decelerate solely by mechanical losses between the two angular speeds, the same test rig was used (Figure 32) but the motor was accelerated by blowing an air jet to the periphery of the motor and a stopwatch was used to measure the time to drop from 285 to 270rpm.

## 3.2. Controller Development

This section describes the efforts to develop the controller for the developed motor. The design of the motor controller was an iterative process where different concepts were developed, prototyped, fabricated and tested. Finally, the best concept was implemented into the car and only this one is described herein.

### 3.2.1. Conceptual design

In an electric propulsion system, the controller has the same importance as the motor itself, in the motor controller lies the capability of managing when and how much current is applied to the motor's phase terminals. Being the development and construction of the motor controller a mandatory rule for battery electric prototypes in SEM regulations, after the motor was built, most of the efforts went to its development in the Aero@UBI team SEM 2105 participation. Since the beginning of the SEM project in late 2013, it was found great potential on the FOC concept. To first try this control strategy, a development kit from Texas Instruments composed by the LAUNCHXL-F28027F and the BOOSTXL-DRV8301 was bought and tested. With this

solution, it was realized the complexity of implementing the FOC concept. So, due to the lack of time and the programming skills available, the chosen control strategy concept had to be moved towards a simpler solution.

The conceptual design of the motor controller results from the implementation of various concepts and some features present in other controllers. Here is a list of the implemented concepts:

- **Modular** - divide the controller in subparts so they can be replaced in case of damage or improved versions of each module is developed later on;
- **Shoot through Protection** - a short-circuit called shoot-through occurs when both switches of a half-bridge are on. In spite of this being not an intended condition, it can happen due to logic propagation delay or due to the time that the MOSFETs require to charge or discharge the gates capacitance and change its state. If this shoot through condition is verified, the current flows directly from VCC to GND wasting energy and burning the circuit. So, the implemented concept is based in creating the half bridges driving signal through the use of two optocouplers to drive the MOSFETs as described by [25]. To implement this concept, two logic bits are used to control each half bridge. The two optocouplers for the high side and low side MOSFETS are connected to the control bits terminals but with reverse polarities to their LED. So, one LED will light up when the control bits have different logic levels. But if both bits have the same logic level no optocoupler will work and, thus, no MOSFET will be turned on;
- **Programmable Logic Device** - the commutation scheme can be easily implemented into a Programmable Logic Device (PLD) due to the fact that the signals from hall effect sensors can be read as a word of 3 bits that can be “computed” through logic gates and generate a corresponding logic output to control the three phase half bridges. [23];
- **Hysteric Control** - due to that the vehicle driving strategy was to keep constant velocity, one simple solution was to keep the motor operating at a constant torque which means that the current should be kept at a constant value as well. The concept here is to compare the current to the desired torque level signal and switch it off if it is too high and switch it on again if it is too low;
- **N-Channel MOSFETs** - in spite of being more difficult to drive, N-Channel MOSFETs are used in both sides of the half-bridges, they have a lower internal resistance and can deal with a higher current;
- **60 Degree Commutation Scheme** - during the development of the controller development, it was found that the presence of the BEMF was very important to limit the current in the phase. So, it was thought that by switching the phase in a 60 degrees commutation, rather than the typical 120 degree commutation it would be easier to control the phase current level. By turning the phase on only 30 degree from its BEMF

peak, the current gradient is smaller and thus the switching frequency is also smaller. In Table 5 is shown the switching sequence.

Table 5 - Switching sequence for 60-degree commutation

INPUT			OUTPUT					
A	B	C	A_H	A_L	B_H	B_L	C_H	C_L
0	0	0	-	-	-	-	-	-
0	0	1	0	0	0	0	1	0
0	1	0	0	0	1	0	0	0
0	1	1	0	1	0	0	0	0
1	0	0	1	0	0	0	0	0
1	0	1	0	0	0	1	0	0
1	1	0	0	0	0	0	0	1
1	1	1	-	-	-	-	-	-

This commutation scheme only works with the center of the motor's star windings connected to a zero-voltage potential created between two capacitors that connect to the DC bus. From the multilevel inverters came the concept that a third level of voltage,  $V_{DC}/2$ , is created in the center of two capacitors connected in series between the  $V_{DC+}$  and  $V_{DC-}$ . This configuration allowed to apply a smaller electromotive force to each phase and thus an easier control of the current level and, at the same time, ensured that only the phase that can better produce torque is energized. In Figure 33 it is shown the graphical representation of the implemented 60-degree commutation scheme.

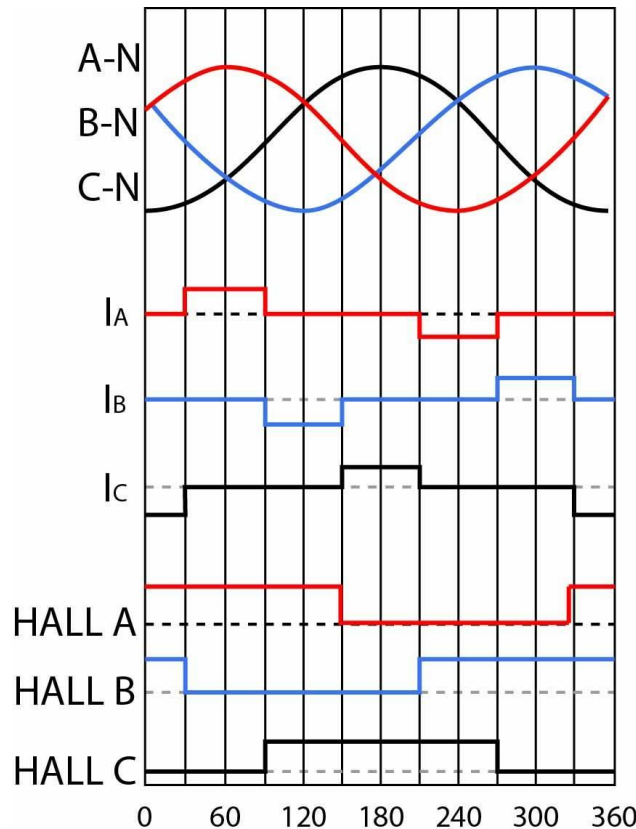


Figure 33 - Graphical representation of the 60-degree commutation scheme

### 3.2.2.Circuit Design and Component Selection

Form the concepts to be implemented into the motor controller from Section 3.2.1 a conceptual schematic was created. From Figure 34 the necessary modules were designed and the components selected.

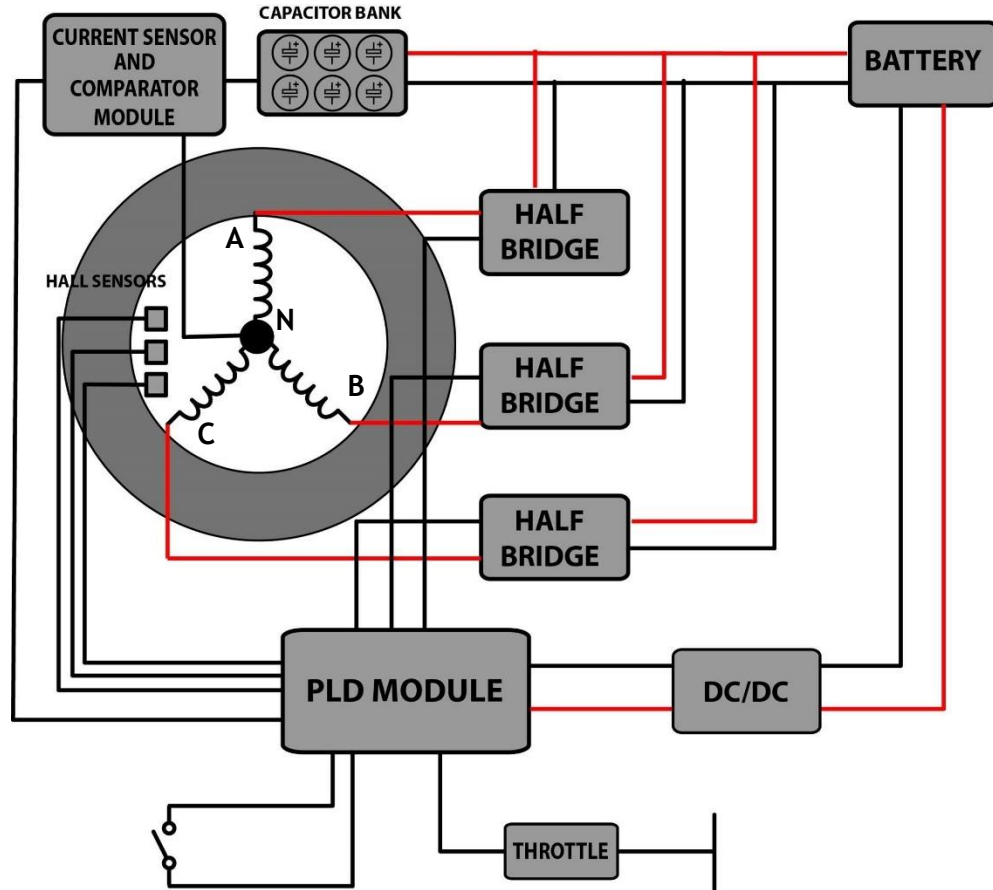


Figure 34 - First controller concept design

A

#### 3.2.2.1. Half-Bridge Module

The inverter is composed by three half-bridge modules. Each of these modules are driven by the corresponding 2-bit logic control signals, one to control the high side MOSFET of the half bridge and the other controls the low side, the control signals are complementary.

##### 3.2.2.1.1. Gate Drive Optocoupler

The ACPL-H342 is an optically-isolated IGBT or MOSFET gate driver (see Table 6 for its specifications). This integrated circuit is used to isolate the TTL logic input signal from the high-power electronics and also allows the amplification of the current supplied to drive the MOSFET gate leading to a smaller turn-on transient times of the MOSFET.

Table 6 - Specifications for the Avago ACPL-H342 Optocoupler

	Specification	Symbol	Value
	Led Forward Voltage	Vf	1.2V
	Led Forward Current	If	10mA
	Maximum Peak Output Current	Ipeak	2.5A

The input for this component should be driven by led current-limiting resistor,  $R_s$ , and calculated according the following equation:

$$R_s = \left( \frac{V_{sig} - V_f}{I_f} \right) \quad (32)$$

Where,  $V_{sig}$  is the input voltage  $V_f$  is the led forward voltage and  $I_f$  is the led forward current. From Equation (32) the resistor value to use should be 316 Ohm but the use of a commercial available value was preferred and the next closest value of 330 Ohm resistor was used.

### 3.2.2.1.2. Shoot-Through Protection

The shoot-through protection circuit is shown in Figure 35 circuit and came from [25] where a capacitor is added in parallel with the two optocouplers and the charging time of the capacitor induces a delay whenever the input of the half-bridge module changes. This ensures the complementarity of the 2-bit signal input.

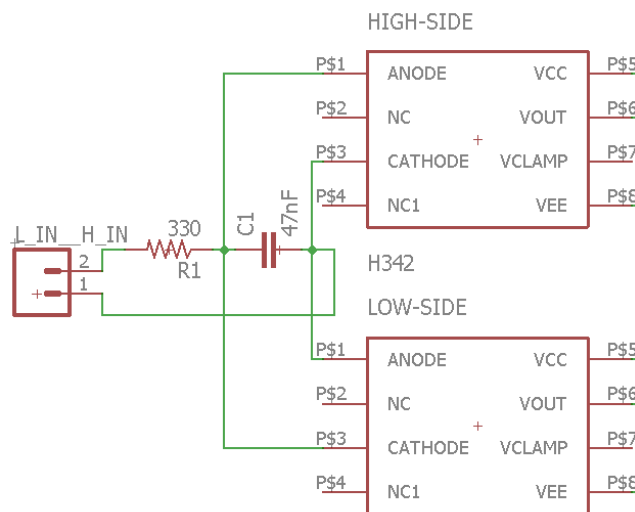


Figure 35 - Shoot-through protection circuit

This delay can be calculated from the equation (33)

$$C_s \approx \left( \frac{t_{delay}}{R_s} \right) \left( \frac{V_{sig}}{2 V_f} \right) \quad (33)$$

Where  $C_s$  is the capacitor capacitance to obtain a desired  $t_{delay}$  between the MOSFETs switch states given the  $V_{sig}$ ,  $R_s$  and  $V_f$ . Choosing a  $t_{delay}$  of 8.5µs a capacitor of 0,0537µF should be used but the closest value commercially available was 0,047µF which should give a  $T_{delay}$  of 7,5µs.

### 3.2.2.1.3. MOSFET

To convert a low-power signal into an amplified high-power output a power switch is needed. The choice was MOSFETs because they are widely used for low-voltage motor controllers as they have a constant low level resistance when they are fully on.

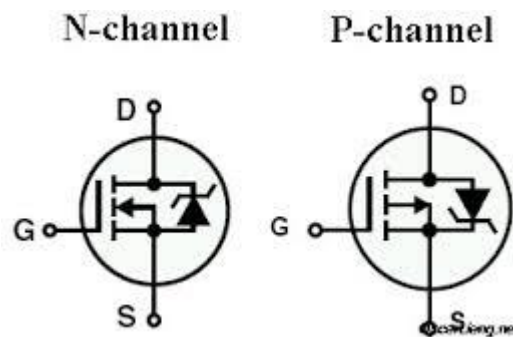
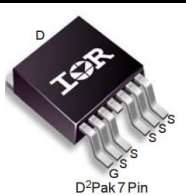


Figure 36 - Electrical symbol of an N-channel and P-channel MOSFETs

In Figure 36 the two types of MOSFETs available, N-channel and P-channel are shown. In most motor controllers, only N-channel MOSFETs are used because they offer smaller values of on resistance than the P-channel MOSFETs. MOSFETS have three terminals: a gate, a drain and a source. A gate voltage, measured in respect to the source, is applied to the gate and when a threshold voltage is achieved the current starts flowing from the drain to the source. As the gate voltage rises, the resistance from the drain to the source decreases and the fully on state is achieved when the gate voltage is about 8-10V. Normally a N-channel MOSFET is connected to the low-side of the circuit, the gate is the input pin, the source is connected to de negative DC bus and the drain is the connected to the circuit's load.

The MOSFET chosen was the AUIRFS8409-7P (Table 7). It was found to be the best compromise in terms of internal resistance, price and gate capacitance. The AUIRFS8409-7P also have a package that can be easy soldered.

Table 7 - Specifications for the AUIRFS8409-7P N-channel MOSFET

	Specification	Symbol	Value
	Drain to Source Voltage	$V_{DSS}$	40V
	Drain to Source Resistance typ.	$R_{DS(ON)}$	0,55mΩ
	Drain to Source Resistance max.	$R_{DS(ON)}$	0,75mΩ
	Continuos Drain Current, $V_{GS}$ 10V	$I_D$	240A

### 3.2.2.1.4. Bootstrap

When a N-channel MOSFET is used in the high side of a half-bridge the drain should be connected to the positive DC bus and the source is connected to the load. Because the gate voltage must be 8-10V higher than the source voltage. A bootstrap is a simple way of creating an elevation of the voltage to drive the gate of the N-channel MOSFET used in the high side of the half-bridge. This is accomplished in two stages (see Figure 37): in the first stage, the low-side MOSFET is turned on, creating a 12v drop across the bootstrap's capacitor, charging it. On the second stage, when the high-side MOSFET is turned on, the bootstrap's capacitor stored voltage is used to keep the high side MOSFET gate 12V above the its source electric potential level. The capacitor to be used should have a value significantly higher than the gate capacitance to allow for the high driving voltage to remain on the driven gate. The presence of the diode connecting to the +DC bus terminal prevents the capacitor from discharging from being connected to this terminal by the driving optocoupler.

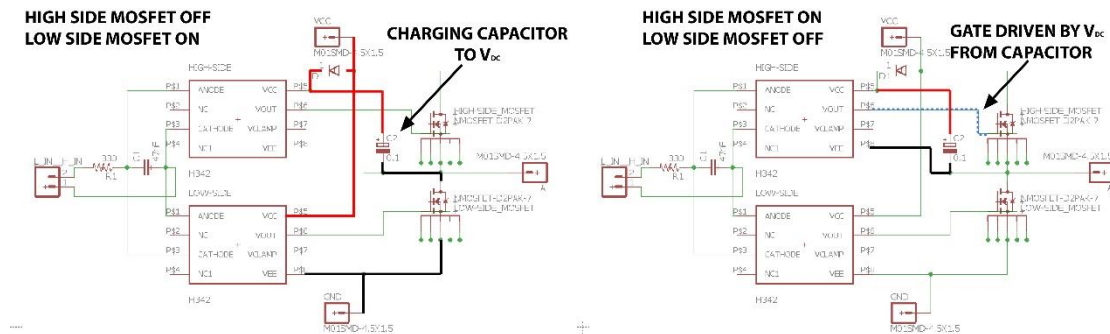


Figure 37 - Bootstrap Operation

### 3.2.2.1.5. Bus Capacitor

A high capacitance bus capacitor is used to source and sink high instantaneous currents to and from the half-bridges. A 1000 $\mu$ F 25V capacitor that we have available was used in this module.

### 3.2.2.2. Current Sensor and Comparator Module

In the current sensor and comparator module, the current is measured and compared to a torque command level that is proportional to the motor current. The torque command signal is mandated by the driver (using a variable resistor) which is compared to the current signal from the current sensor. This will generate a phase current level control PWM signal that is logically multiplied with the phase commutation signal that goes to the half-bridge module to limit the current that is supplied to the motor in accordance with the torque command signal.

### 3.2.2.2.1. Current Sensor

The best point to measure the current in this controller configuration was between the capacitor bank module and the center of star of the motor, all the current supplied to the motor windings is passing through this point (shown in Figure 34).

It was decided to use two unidirectional current sensors, the ACS770-50U IC (see Table 8), one measuring positive current and the other the negative current. With this current sensing configuration, it was possible to have a sensed output voltage that was proportional to the phase current, starting from 0V, when the current direction is through the normal sensing direction of the sensor and when the current direction is the opposite to the normal sensing direction of the sensor output value remains at 0V.

Table 8 - ACS770-50U IC specifications

	Specification	Symbol	Value
	Primary Current Sampled	$I_p$	50A
	Sensitivity (typ.)	-	80mV/A
	Current Directionality	-	Unidirectional

### 3.2.2.2.2. Current Comparator

The LM311 was used to compare the current signal from the current sensor and compare it with the torque command signal. If the sensed current voltage is lower than the torque command voltage signal the comparator will send a 1 to an AND gate that puts a 1 on the current level control PWM signal. If, by the other hand, the sensed current voltage is higher than the torque command voltage signal the comparator will send 0 to the AND gate that, independently of the current sensed by the other sensor will set the PWM to 0.

### 3.2.2.3. PLD Module

The PLD module has the function of implementing the switching sequence shown in Table 5 depending on the hall effect sensors inputs. This was done by using Karnaugh maps to simplify the Boolean algebra expressions. To the output expressions, the PWM signal generated by the current sensor and comparator module was multiplied using an AND logic operator. The final expressions used are:

AH=A&!B&!C&PWM;  
AL=!A&B&C&PWM;  
BH=!A&B&!C&PWM;  
BL=A&!B&C&PWM;  
CH=!A&!B&C&PWM;  
CL=A&B&!C&PWM;

### **3.2.2.3.1. Motor Position**

The motor position is determined using three hall effect sensors mounted in the motor's stator. These Hall effect sensors are operated by the magnetic field from the motor permanent magnets, they respond to South (switch on) and North (switch off) and they must be positioned 120 electrical degrees apart.

### **3.2.2.4. Capacitor Bank Module**

The capacitor bank connected to the center of the motor star windings is used to store the energy needed to drive the motor. The current flows to and from the capacitors to the motor phase winding that is connected to the DC bus at each instant, so the capacitors should have the highest capacitance as possible, limited by their weight and volume.

### **3.2.3. Implementation**

From the concepts and components chosen on section 3.2.2, their implementation was made in five steps. The first step was to design the schematic of each individual module on an electronic CAD software. The chosen software was the EAGLE from CADSOFT/AUTODESK, it is free for students and the only limitation is that a maximum of one schematic page and about 100X60mm PCB size can be used per project, which was sufficient because the controller is divided in smaller modules. The second step was to print the layouts from EAGLE, with the components footprint size and position in photographic paper. The third step was to transfer the circuit design from the photographic paper to the copper plating, of the FR4 glass-reinforced epoxy sheet, with a clothes iron. After that, the photographic paper was stuck to the PCB. So, it was soaked in water to dissolve de paper leaving only the toner behind. In fourth step, the excess copper, that was not covered by the toner, was removed with ferric chloride. The fifth and last step was to solder the components into the board.

Because through-hole and surface mounted components were used in the same board the pads of through-hole components were bent so they could be used as surface mounted. The schematics and the final built modules are shown in the next Sections.

### 3.2.3.1. Half-Bridge Module

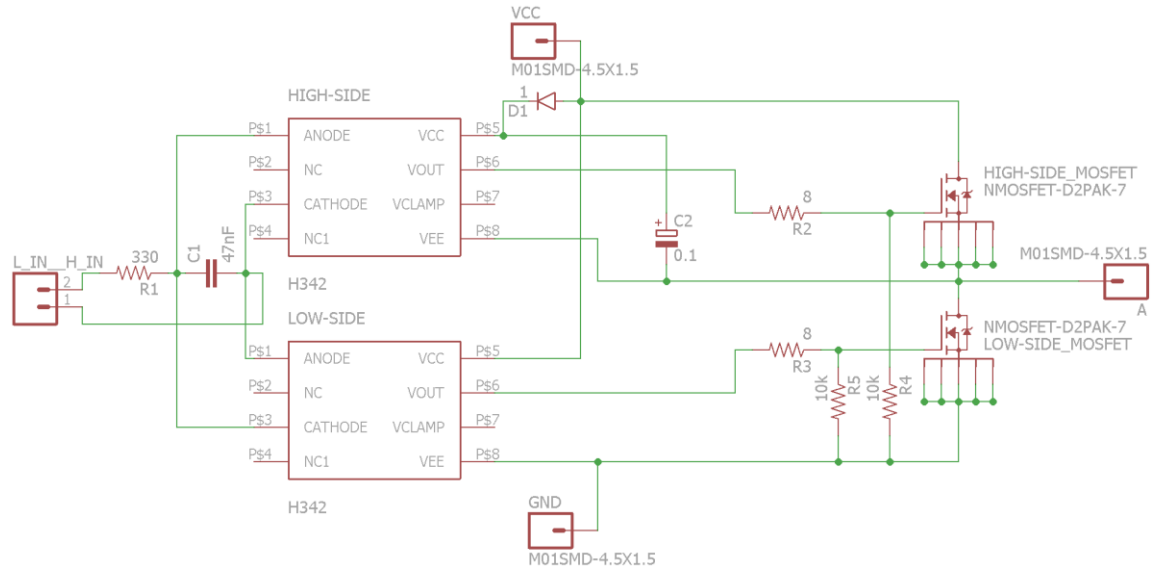


Figure 38 - Half-Bridge Module Schematic

The Figure 38 shows the half-bridge modules schematic. The Half-Bridge Module layout and built are shown in Figure 39. To simplify the manufacture process of this module and to enable its implementation in a one side PCB, a wire connection was added. After the manufacture of the first version of this module (V0.3), a modification on the bootstrap was made, the layout of the module updated and the PCB was corrected (V0.6).

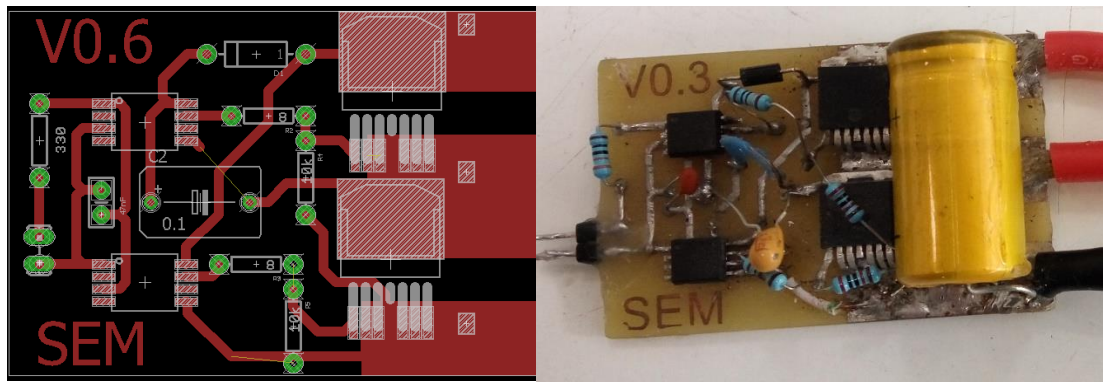


Figure 39 - Half-Bridge Module board layout(left) and built(right).

### 3.2.3.2. Current Sensor and Comparator Module

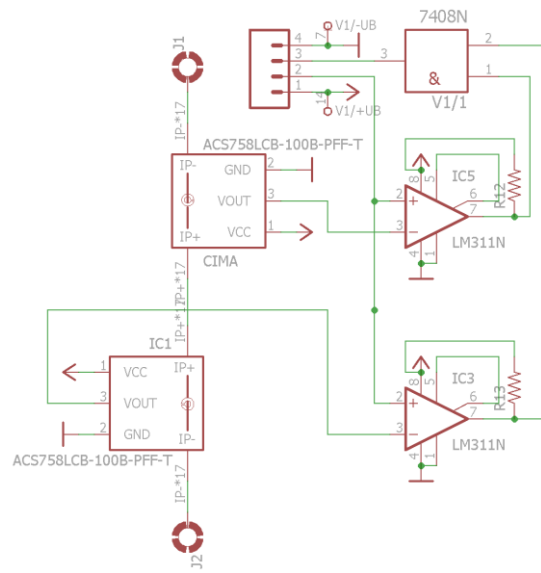


Figure 40 -Current Sensor and Comparator Module Schematic.

The Figure 40 shows the Current Sensor and Comparator Module schematic. The Current Sensor and Comparator layout and assembly module are shown in Figure 41.

Figure 41 -Current Sensor and Comparator Module layout(left) and built(right).

50

### 3.2.3.3. PLD module

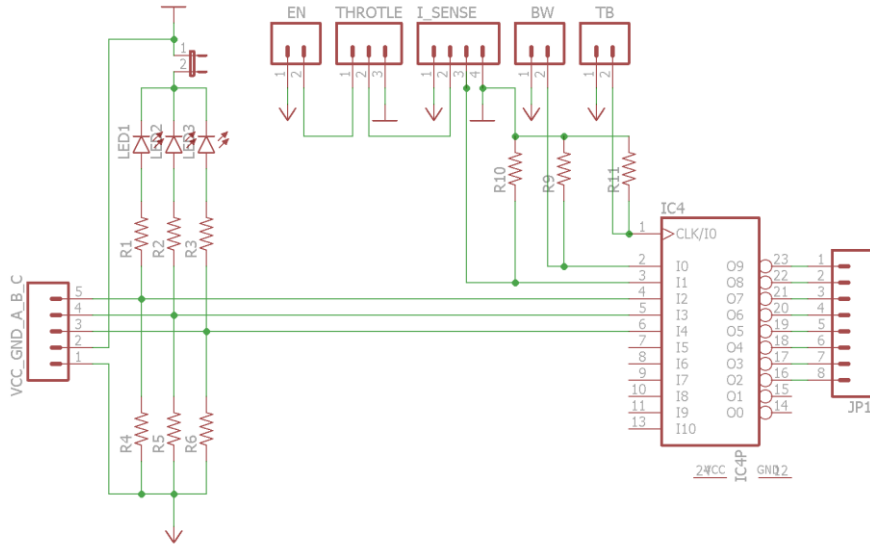


Figure 42 - PLD Module Schematic.

Figure 42 shows the PLD Module schematic. The PLD Module layout and built module are shown in Figure 43. In this module, it was intended to add two more functions to the actual controller: a backwards function to reverse de motor's direction of rotation and a turbo function that adding a fourth half-bridge in the center of the motor star terminal should allow the motor to be driven by the double of the DC bus voltage. At the end, these functions never were implemented but the circuit board with those connections it was used.

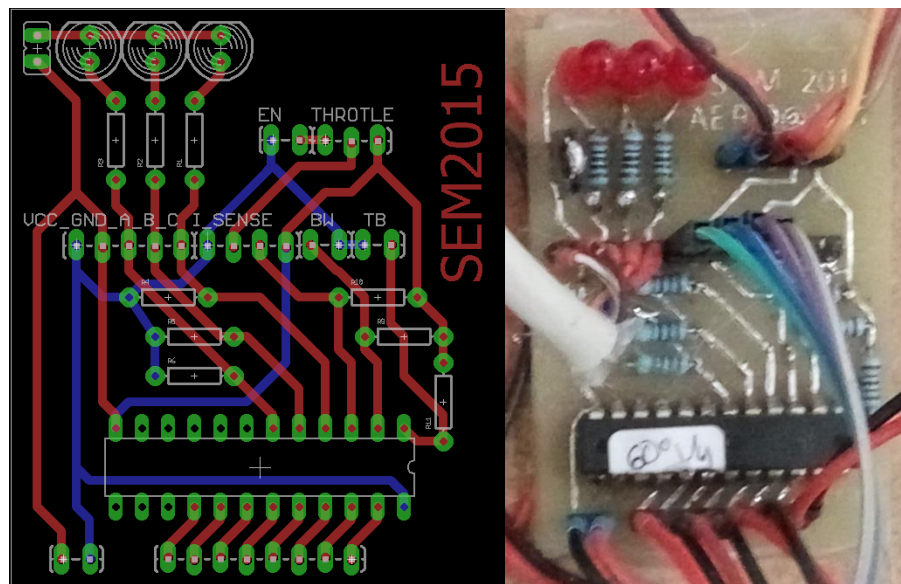


Figure 43 - PLD module layout(left) and assembled(right)

### 3.2.3.3.1. Motor Position Sensors

The three hall effect sensors were pre-positioned with the correct angle between them requiring the correct positioning of just of the three sensors

The correct positioning of the hall effect sensors is extremely important, it will have a big influence on the motor's operation. To place the hall effect sensors, a laser cut piece of plywood was built to hold and space the sensors. The sensors should be 120 electrical degrees apart, which, in the developed motor corresponds to 6 mechanical degrees. Having guaranteed the correct spacing between the three sensors, only one of the sensors needs to be aligned.

The positioning the hall effect sensor on the stator was made with an oscilloscope to ensure that the output signal of the hall effect sensor was coincident with the positive part of the BEMF from the corresponding phase. Figure 44 shows the final position of the hall effect sensors.

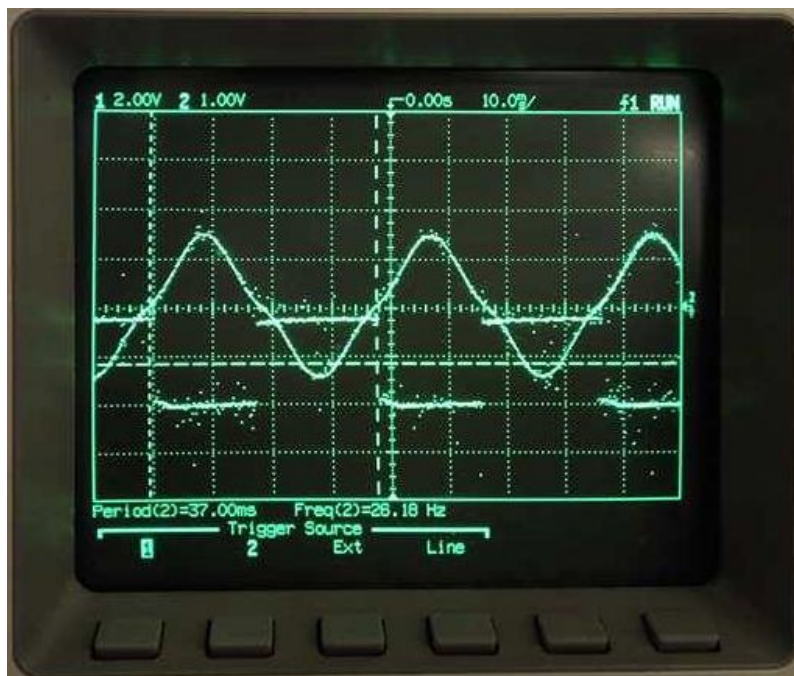


Figure 44 - Hall Effect Sensors positioning.

### 3.2.3.4. Capacitor Bank Module

Figure 45 shows the Capacitor bank that is connected to the center of the star. These capacitors are connected in three parallel groups of two capacitors in series. They are kept together with a 3D printed PLA piece (shown in the white color).



Figure 45 - Capacitor Bank Assembled

### 3.2.4. Controller Testing

After the fabrication of all the modules of the controller, they were tested. In the following Sections, the experiments are described.

#### 3.2.4.1. Current Limiting Function

To evaluate the controller's current level limiting function operation, the motor and the controller were connected. Using the controller to make the rotor spin and braking it by hand, with an oscilloscope to watch one phase voltage and the current measurements, it was possible to see how the controller regulates the current. Figure 46 is shows the test rig for the current limiting function operation check.

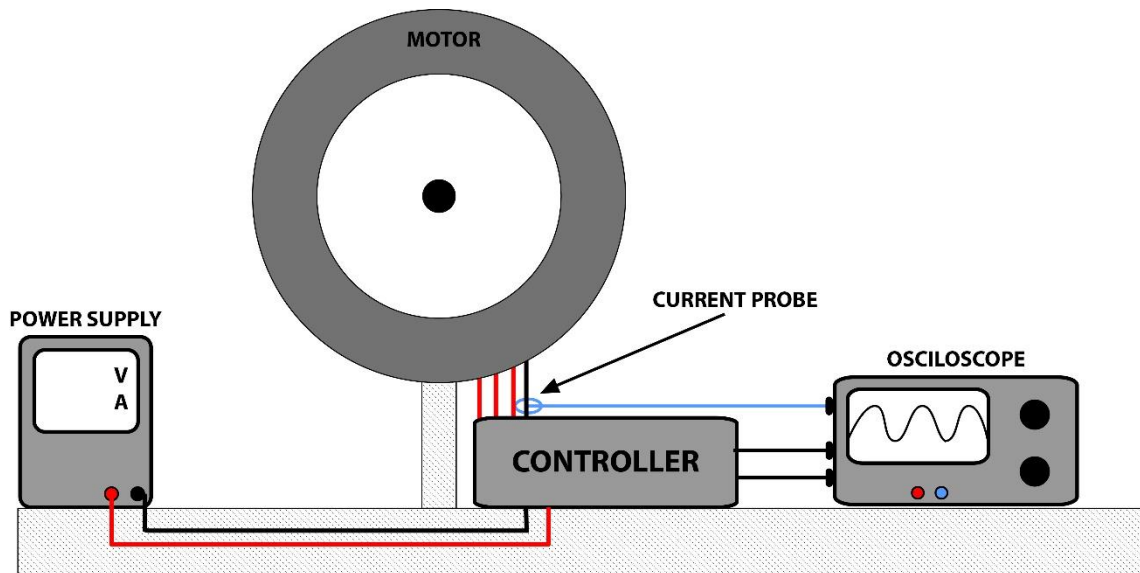


Figure 46 - Motor-Controller system test rig schematic.

### 3.2.5. Controller and Motor Testing

After the fabrication and validation of the controller current limiting function operation, the motor and the controller were tested together, as a system, to evaluate its performance. For these tests, the motor and controller were mounted on a test rig like they will be installed on the Aero@UBI car prototype. For these tests, the energy was supplied from a regulated bench power supply that shows the voltage and current sourced to the motor and controller. The motor speed was calculated from the frequency of the BEMF signal monitored on the oscilloscope.

#### 3.2.5.1. No Load Current

A test with no load applied to the motor was done to compare the power needed to keep the motor spinning at 277 rpm with the motor's previously measured losses. In this condition, the energy consumed is only used to keep the motor running. In Figure 46, the test rig for the no load current test is shown.

#### 3.2.5.2. Loaded System Testing

The next step was to apply a load to the motor. This load should represent the torque applied on the motor when it is running the SEM car prototype on the track, and from Table 3. Figure 47 shows the test rig used in this loaded motor system testing. The torque applied to the motor was accomplished by using two weights hanging in the ends of a leather strap. The leather strap, in contact with the rotor, creates friction that is proportional to the  $m_2$  weight. The weight  $m_1$  must be higher than  $m_2$  and it was used to tare the scale before the motor is run.

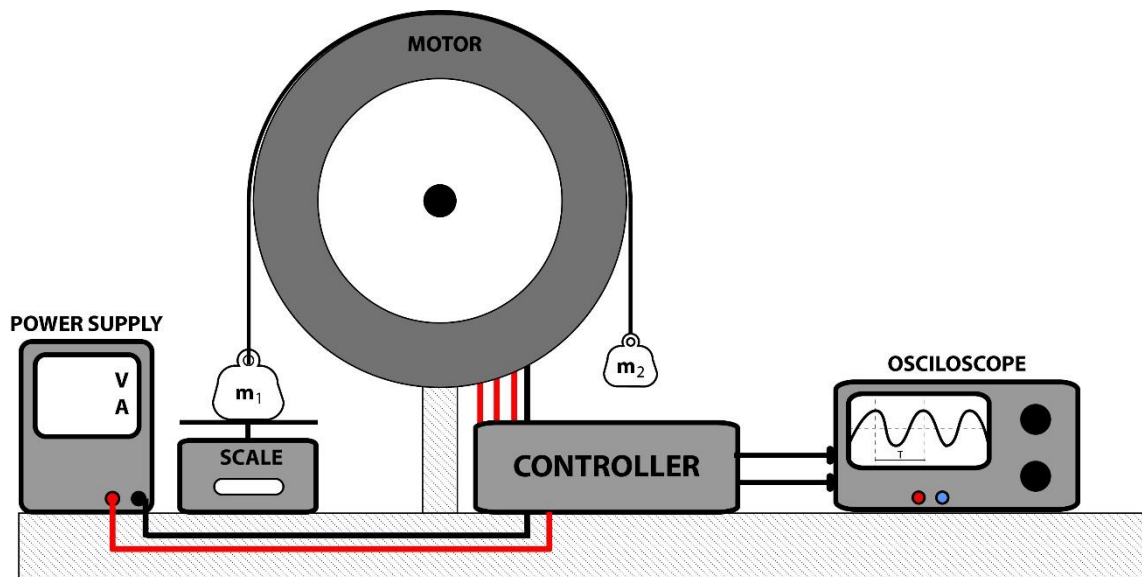


Figure 47 - Schematic of the test bench used for load measurements

### **3.2.5.3. Load Testing with TI C2000 and DRV8301Controller**

The previous test was repeated, this time the designed controller shown in Figure 47 was replaced by the TI commercial solution, the C2000 processor and the DRV8301 inverter controller.



# Chapter 4

## 4. Results

The present chapter the results of the tests made to the motor and controller.

### 4.1. Motor Testing

#### 4.1.1. Back Electromotive Force

Figure 48 shows the experimental BEMF measured in the oscilloscope using the test rig described in Section 3.1.5.1.

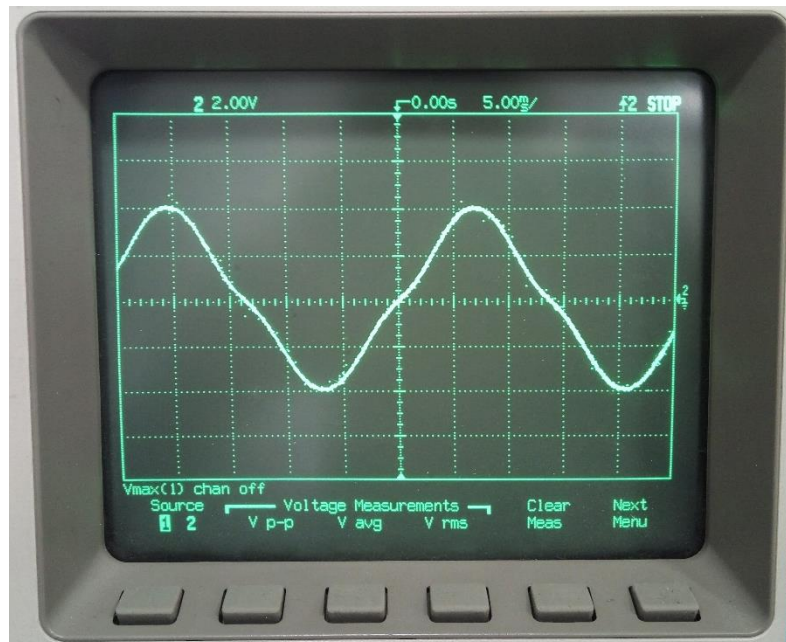


Figure 48 - BEMF measurement

Figure 49 illustrates the measured voltage waveform compared to a sinusoidal waveform. The measured motor BEMF shows a significant difference against the desired sinusoidal wave, this is attributed to the difference between the magnet width (12mm) and the and wave coil width around the magnet (23.5mm), making the linearity of the BEMF crossing the zero voltage disappear. Once the magnet flux is inside the coil, it does change until the magnet it reaches the other end of the coil, this time gap reflects in the drop of the BEMF gradient.

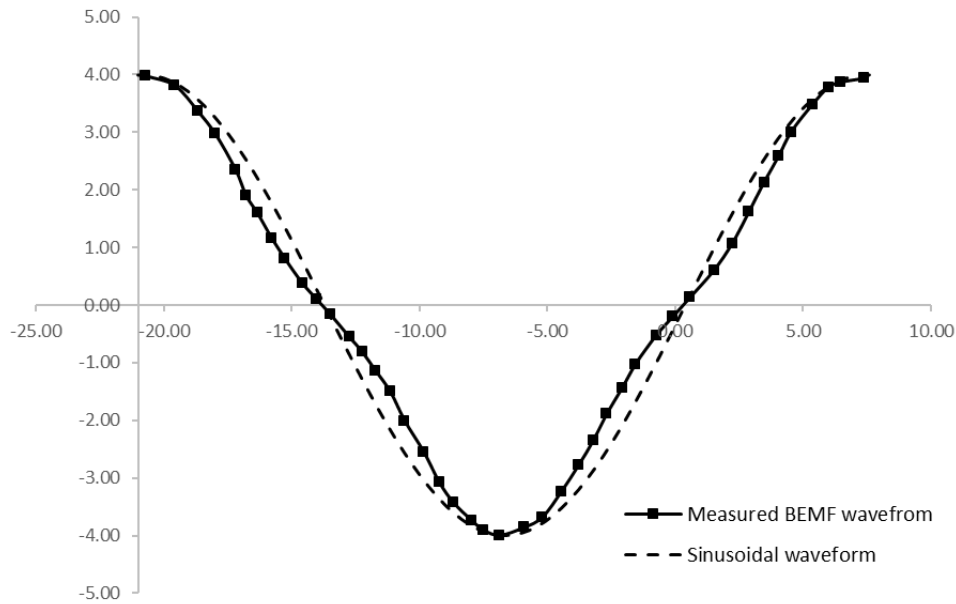


Figure 49 - Measured voltage waveform vs sinusoidal waveform

#### 4.1.2. Motor Mechanical Losses

##### 4.1.2.1. Motor Rotor's Moment of Inertia

Figure 50 shows the experimental motor rotor's moment of inertia measurements using the test rig described in Section 3.1.5.2.1.

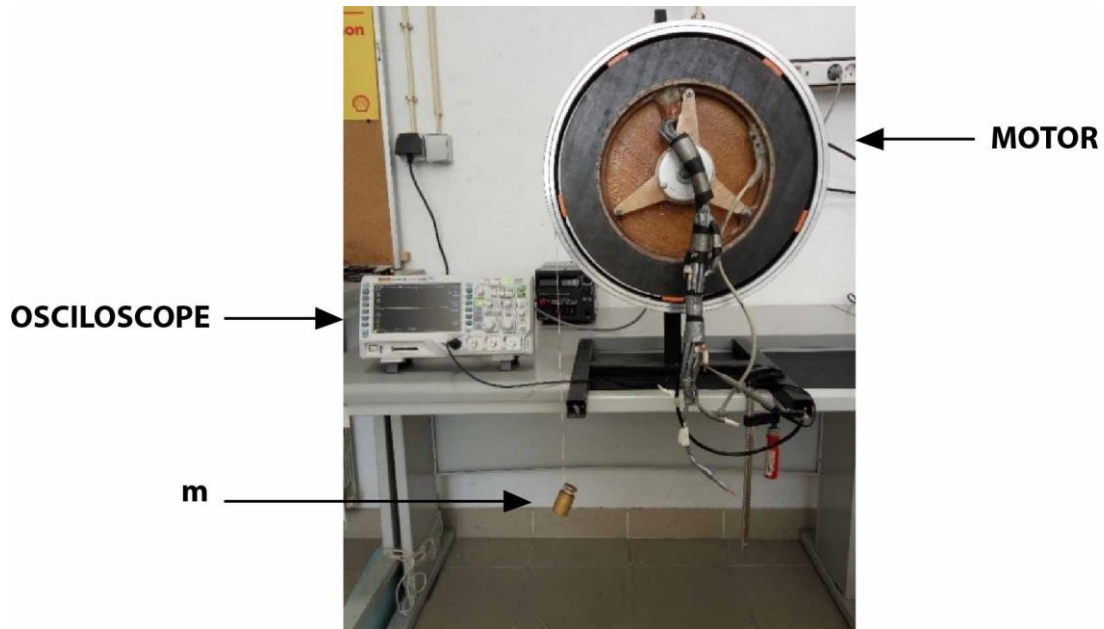


Figure 50 - Motor of inertia measurement test rig according to section 3.1.5.2.1

Table 9 shows the measurements and the results according to formulae given in Section 3.1.5.2.1 calculations of the tests data. To find the rotor moment of inertia, which was used

to obtain the measurements of kinetic energy used later to measure the mechanical losses of the motor according to description of Section 3.1.5.2.2. The measured moment of inertia of the motor rotor is  $0.240 \text{ kgm}^2$ .

**Table 9 - Rotor's moment of inertia measurements**

Test	P[kg]	h[m]	freq[Hz]	$\omega$ [rad/s]	I[kgm^2]
1	0.1	0.75	7.7	2.409	0.249
2	0.1	0.75	6.7	2.094	0.331
3	0.05	0.75	5.3	1.676	0.260
4	0.05	0.75	5.3	1.676	0.260
5	0.15	0.75	10.0	3.142	0.217
6	0.15	0.75	9.7	3.037	0.233
7	0.15	0.75	10.0	3.142	0.217
8	0.2	0.75	11.3	3.560	0.224
9	0.2	0.75	12.0	3.770	0.199
10	0.2	0.75	11.7	3.665	0.211
					Average <b>0.240</b>

#### 4.1.2.2. Motor Mechanical Losses Measurement

Using the measured moment of inertia of the motor rotor of  $0.245 \text{ kgm}^2$ , and the measured time to decelerate from 285 rpm to 270 rpm, the motor's mechanical power loss near the design point were obtained. In Table 10 are shown the results of ten repetitions of the test described in Section 3.1.5.2.2 and the motor's average mechanical power losses. The data are consistent with the average result of 2.558 W for the motor's mechanical power loss near the design point.

**Table 10 - Motor mechanical losses measurements**

Test	E_285[J]	E_270[J]	t_285-270[s]	P_Loss[W]
1	106.965	96.002	4.270	2.567
2	106.965	96.002	4.650	2.358
3	106.965	96.002	4.310	2.544
4	106.965	96.002	4.250	2.580
5	106.965	96.002	4.320	2.538
6	106.965	96.002	4.120	2.661
7	106.965	96.002	4.210	2.604
8	106.965	96.002	4.420	2.480
9	106.965	96.002	4.210	2.604
10	106.965	96.002	4.150	2.642
				<b>Average 2.558</b>

## 4.2. Controller Testing

### 4.2.1. Current Limiting Function

In Figure 52 it is shown how the current is limited with the developed controller as described in Section 3.2.4.1, the hysteretic control limits the current within an upper and a lower

hysteresis band. It is, also, possible to observe that the 60 degree commutation is symmetric with the BEMF peak and the commutation frequency is smaller near the BEMF peak.



Figure 51 - Current limiting function measurements

### 4.3. Controller and Motor Testing

#### 4.3.1. No Load Current

Figure 52 shows the experimental data corresponding to the motor-controller system tested as described in Section 3.2.5.1.

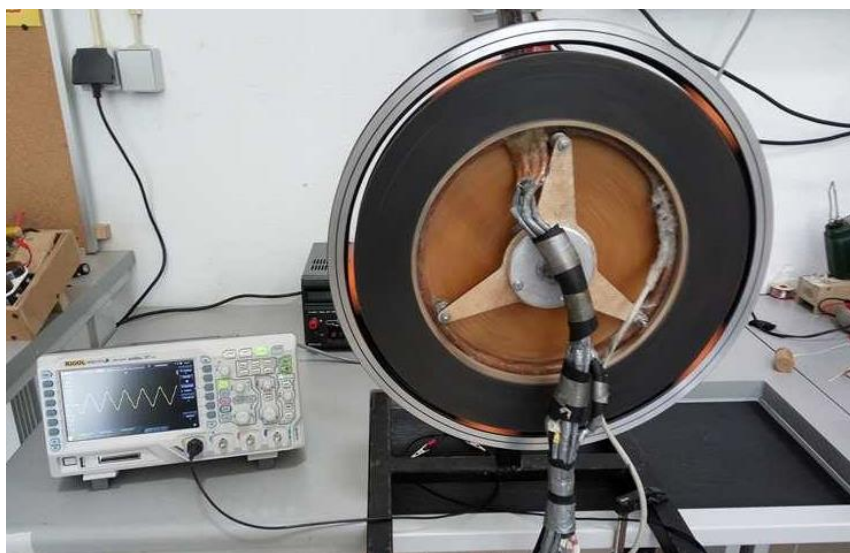


Figure 52 - No load current measurement

The motor rotation speed was kept around the 277rpm. Figure 53 shows the results of the motor measurements with no load applied, the total power required to spin the motor is about 5.985 W. Please note that in this value are included the power consumption of the controller and motor mechanical losses.

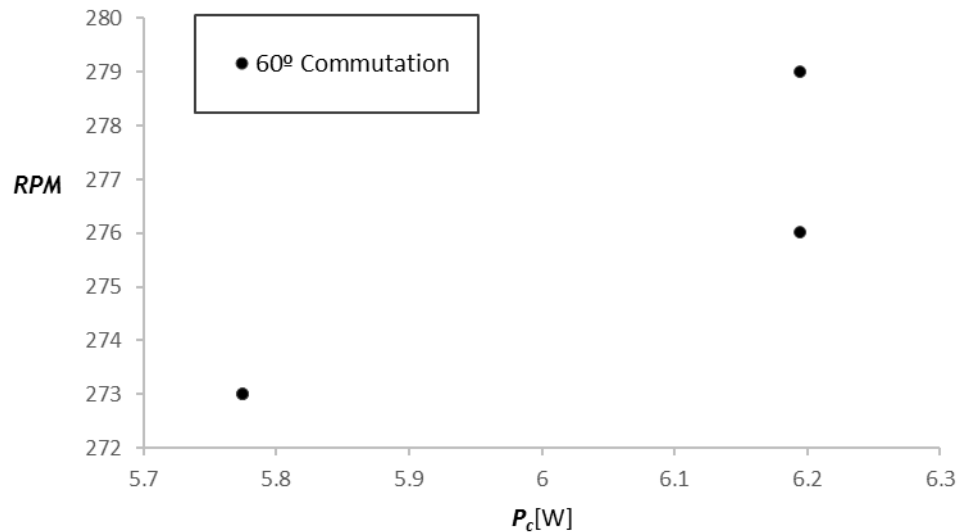


Figure 53 - Motor-Controller system efficiency experimental results with no load

#### 4.3.2. Load Current

Figure 56 shows the experimental data corresponding to the motor-controller system tested in the test rig described in Section 3.2.5.2.

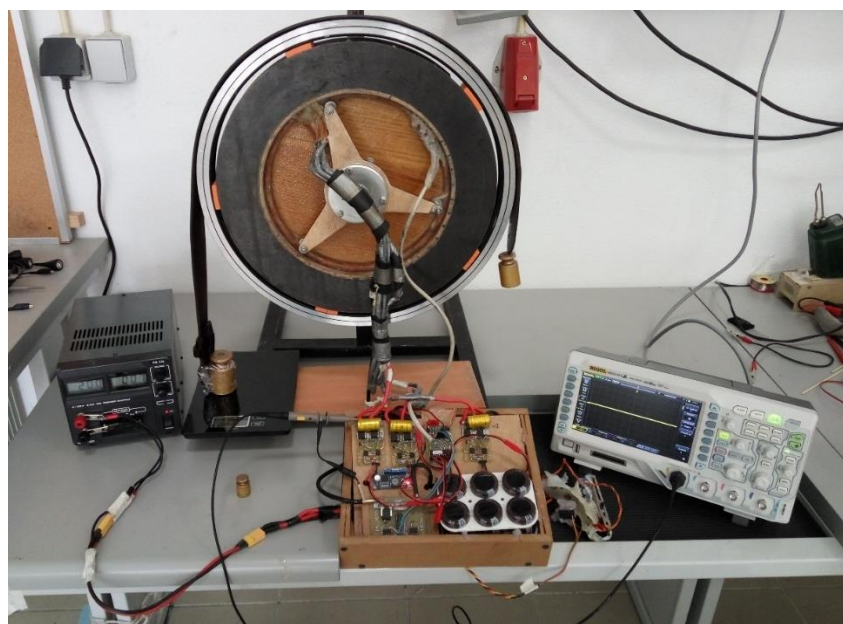


Figure 54 - Load current measurement

The motor rotation speed and load was kept close to the design 277 rpm and 0.510 Nm, respectively. From Figure 55 were the tests results of the motor-controller system efficiency are presented. The designed system has an efficiency over 80% through the design point.

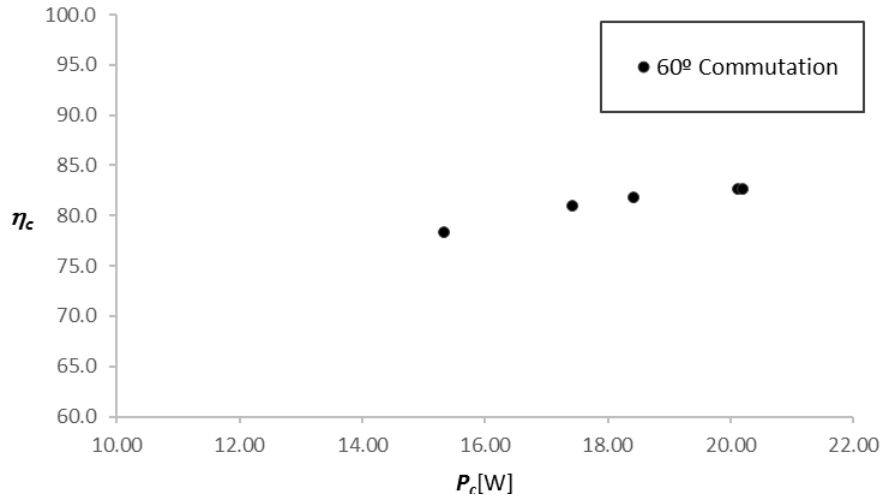


Figure 55 - Motor-Controller system efficiency experimental results of the designed controller

#### 4.3.3. Load TI C2000 and DRV8301

Figure 56 shows the experimental data corresponding to the motor-controller system tested in the test rig described in Section 3.2.5.3. The motor rotation speed was kept close to the design 277rpm. The data corresponding to the use of Texas Instruments DRV sinusoidal FOC controller are also presented for comparison. When using the TI controller, 90mH choke inductors are connected in series with the motor phase terminals to limit the current ripple and improve the sensorless TI controller sensing. It is seen that the peak efficiency of the developed 60° commutation controller is quite near the efficiency of the state of the art commercial sinusoidal field oriented controller.

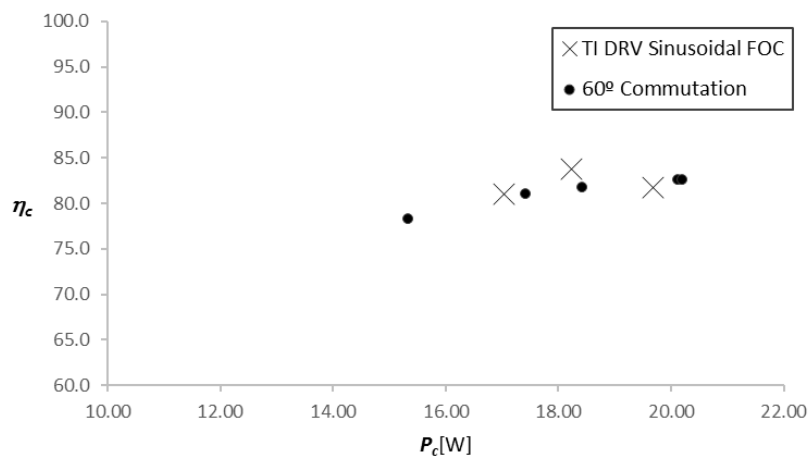


Figure 56 - Motor-Controller system efficiency experimental results comparison between TI DRV and the designed controller

#### **4.3.4. SEM Vehicle Prototype on Track Performance**

The SEM 2015 on Rotterdam flat track result was 331 km/kWh, corresponding to the 19th place in the battery electric prototypes category. Only 33 vehicles achieved a result on the track. Comparing this 2015 SEM Europe result with the other SEM battery electric prototypes around the globe, our vehicle got a 24th result in 57 vehicles. The top performing vehicle in 2015 was the Technische Universitaet Muenchen with 863 km/kWh. One cannot attribute the result to the motor controller system alone since the vehicle aerodynamics and mechanical losses are also in play.

In our next participation, in 2017, the vehicle body and chassis were changed. The result improved to 372 km/kWh. Corresponding to the 11th place in 39 battery electric vehicle prototypes participating in SEM Europe in London despite track having a steep 5% uphill incline that was probably not favorable to our current propulsion system. It is noteworthy to mention that all teams except ours and University Of Applied Sciences Offenburg team were using very similar versions of DC brushed MAXXON motors of about 200W power. The German team got in the 8th place and also uses an in-wheel motor that is similar to our own.



# **Chapter 5**

## **5. Concluding Remarks**

The development of an efficient propulsion system for the Aero@UBI Shell Eco Marathon battery electric prototype was documented. A PMSM in-wheel coreless motor and dedicated controller were designed and prototyped. It was shown that using simple methods and solutions it was possible design and build in-house a motor and controller system from scratch that is able to compete with proven state of the art industry counterparts.

Regarding the motor efficiency as an electrical machine, it is worth of note having only 2.5W of power losses at 277 rpm. But while being driven, the current ripple due to driving the present motor, of very low inductance configuration, from a DC bus, increases the total losses to 4.5W. It is still a very low losses level if one considers that such a motor is expected to be able to withstand a driving power in the order of the units of kW.

The controller itself, despite its simplified design and being only a proof of a new concept, it proved to be capable of driving such peculiar motor as efficiently as the state of the art industry controller.

## **Future Work**

As future work, it is suggested that the developed motor should be further characterized regarding the high-power working limit and respective efficiency.

Significant weight reduction of the current motor can be achieved if the rotors steel plates are replaced by a carbon fiber composite material, while the magnets arrangement being changed to a Halbach array.

Another aspect that should be taken in consideration in the design of a future version of the motor is the possible demagnetization of the magnets, due to excessive winding current induced field in high torque conditions. This could be predicted with a numerical simulation of the motor magnetic flux.



## References

- [1] Colton, Shane William. "Design and prototyping methods for brushless motors and motor control". Diss. Massachusetts Institute of Technology (2010).
- [2] Hanselman, Duane C. "Brushless permanent magnet motor design". The Writers' Collective (2003).
- [3] Nilsson, Christoffer, and Daniel Modrak. "Universal embedded motor control". Diss. Master's thesis, Chalmers University of Technology (2013).
- [4] Hassan, Abu, et al. "Efficiency Comparison of Trapezoidal and Sinusoidal Method for Brushless DC Motor Drive." *Applied Mechanics and Materials*. Vol. 785. Trans Tech Publications (2015).
- [5] "Simulate an AC Motor Drive" [Online] Available: <https://www.mathworks.com/help/physmod/sps/powersys/ug/simulating-an-ac-motor-drive.html?requestedDomain=www.mathworks.com> [Accessed:26-JUN-2017]
- [6] Franquelo, Leopoldo G., et al. "The age of multilevel converters arrives." *IEEE industrial electronics magazine* 2.2 (2008).
- [7] Rodriguez, Jose, Jih-Sheng Lai, and Fang Zheng Peng. "Multilevel inverters: a survey of topologies, controls, and applications." *IEEE Transactions on industrial electronics* 49.4 (2002): 724-738.
- [8] "What is 'Field Oriented Control' and what good is it?" [Online] Available: <http://www.copleycontrols.com/Motion/pdf/Field-Oriented-Control.pdf> [Accessed:26-JUN-2017]
- [9] Lee, Shiyoung, Tom Lemley, and G. Keohane. "A comparison study of the commutation methods for the three-phase permanent magnet brushless dc motor." Pennsylvania State Univ. Berks Campus (2004): 3-5.
- [10] Caricchi, F., et al. "Prototype of electric vehicle drive with twin water-cooled wheel direct drive motors." Power Electronics Specialists Conference, 1996. PESC'96 Record., 27th Annual IEEE. Vol. 2. IEEE, 1996.
- [11] Lovatt, H. C., V. S. Ramsden, and B. C. Mecrow. "Design of an in-wheel motor for a solar-powered electric vehicle." IEE Proceedings-Electric Power Applications 145.5 (1998): 402-408.
- [12] Brown, Jeff. "High Efficiency Permanent Magnet Motor". 2010.

- [13] Wang, Rong-Jie, et al. "Optimal design of a coreless stator axial flux permanent-magnet generator." *IEEE Transactions on magnetics* 41.1 (2005): 55-64.
- [14] "LaunchPoint Technologies Announces New High Efficiency, High Power Density, Halbach Array Electric Motor" [Online] Available: <http://www.prweb.com/releases/high-power-density/electric-motor/prweb2870024.htm> [Accessed:26-JUN-2017]
- [15] Endresen, Fredrik Vihovde. "Electric Motor Development for Shell Eco-Marathon". Diss. Norwegian University of Science and Technology" (2012).
- [16] Nasrin, Lubna. "Improved Version of Energy Efficient Motor for Shell Eco Marathon. Diss. Royal Institute of Technology" (2011).
- [17] Buøy, John Ola. "Development of high efficiency Axial Flux Motor for Shell Eco-marathon. Diss. Norwegian University of Science and Technology" (2013).
- [18] Batzel, Todd D., Andrew M. Skraba, and Ray D. Massi. "Design and Test of an Ironless Axial Flux Permanent Magnet Machine using a Halbach Array" *International Journal of Modern Engineering*: 52.
- [19] Piggott, H. "Brakedrum PM-Alternator Windmill Plans.". UK 1998.
- [20] Piggott, H. "PMG construction manual." The schumacher centre for technology and development", Bourton Hall, UK (2001): 1-49.
- [21] Piggott, Hugh. "How to Build a Wind Turbine: The Axial Flux Windmill Plans". H. Piggott-Scoraig Wind Electric (2008).
- [22] Bumby, J. R., N. Stannard, and R. Martin. "A Permanent Magnet Generator for Small Scale Wind Turbines". Proceedings of ICEM 2006. (2006).
- [23] Van den Bossche, Alex, et al. "Programmable logic device based brushless DC motor control". Power Electronics and Applications (EPE 2011), Proceedings of the 2011-14th European Conference on. IEEE, (2011).
- [24] Jung, Yong-Bae, et al. "Unique axial flux motor design delivers superior torque density". EET-2008 European Ele-Drive Conference International Advanced Mobility Forum Geneva, Switzerland, (2008).
- [25] Colton, Shane William. "Simple Modular Half-Bridge" [Online] Available: [http://web.mit.edu/first/kart/controller\\_rev1.pdf](http://web.mit.edu/first/kart/controller_rev1.pdf) [Accessed:26-JUN-2017]